The Development of Three Dimensional Porous Nickel Materials and their Catalytic Performance towards Oxygen Evolution Reaction in Alkaline Media

by

Zhihao Zhang

Thesis submitted to the

University of Ottawa

in partial Fulfillment of the requirements for

the Master of Applied Science degree in Chemical Engineering

uOttawa

Department of Chemical Engineering

Faculty of Engineering

University of Ottawa

ABSTRACT

As the global energy crisis and challenges with environmental pollution continue, there is an increasing demand for clean and sustainable energy storage and conversion technologies, such as water-splitting electrolysis. Water electrolysis is a process of running an electrical current through water, separating hydrogen and oxygen. Oxygen evolution reaction (OER) is a key reaction in this electrochemical process, and the electrochemical performance of such systems is usually hindered by the slow OER kinetics. To achieve high energy conversion efficiency, the development of efficient OER catalysts is essential. Toward this end, a great deal of research is being done on the use of noble metal oxides as catalysts, such as IrO_2 and RuO_2. However, because of their high cost, a cheap earth-abundant material with a high OER catalytic activity is required. Accordingly, this study focuses on the synthesis of three-dimensional porous structured Ni-based OER catalysts.

A three-dimensional porous Ni meso-foam was developed through a facile high-temperature one-pot synthesis method, and its catalytic activity toward OER was explored. Specifically, the as-synthesized Ni meso-foam material (referred to as raw NMF) has a wire-linked structure and high surface area. A reduction procedure was introduced to obtain reduced Ni meso-foam materials (referred to as NMF-H_2). Raw NMF materials were oxidized in air at 600°C to form a semi-hollow NiO crosslinking phase and were subsequently reduced in H_2 at 300°C, forming a regenerated porous Ni foam material (referred to as NMF-O_2/H_2). The composition and morphology of all materials were

investigated by XRD and SEM, respectively. The SEM image reveals that, in the porous NMF-O_2/H_2, the cross-linked meso-wire structure was maintained and the average pore size was between 0.5–5.0 μm. Electrochemical analysis shows that the OER activity of the Ni foam catalysts follows NMF-O_2/H_2 > NMF-H_2 > raw NMF.

In addition to the NMF-based materials, a Ni/$Ni(OH)_2$ layer-structured electrocatalyst (referred to as Ni_{DHBT}) was developed using a dynamic hydrogen bubble templating (DHBT) method. First, the three-dimensional porous micro Ni/Zn nanoplatelets were constructed in a two-step DHBT deposition method. The Ni/Zn foil was used as a scaffold, featured with the open porous structure and high surface area, for the subsequent electrodeposition of $Ni(OH)_2$. Then, the Zn was etched from the as-prepared Ni/Zn/$Ni(OH)_2$ nanocomposite to obtain the Ni_{DHBT}. The catalytic performance of the Ni_{DHBT} toward OER was evaluated, and the optimal catalysts developed from different electrodeposition potentials was determined.

Upon recognition of the high catalytic activity of NMF-O_2/H_2 and the Ni_{DHBT}, porous structured FeO_x-Nickel meso-foam (referred to as Fe@NMF-O_2/H_2) and FeO_x-Ni/$Ni(OH)_2$-layered structure materials (referred to as Fe@Ni_{DHBT}) were further developed to explore the benefits of FeO_x deposition for its OER catalytic performance. The deposition of FeO_x is achieved by physically mixing FeO_x colloid with NMF-O_2/H_2 and the Ni_{DHBT}, and the electrochemical performance of these materials was examined in 1 M KOH.

Among the developed materials, the best performing catalyst is Fe@Ni_{DHBT} synthesized by loading FeO_x colloid onto the Ni_{DHBT} support. The overpotential for Fe@Ni_{DHBT} to reach 10 $mA{\cdot}cm^{-2}$ is 247 mV, and the corresponding Tafel slope is 48.10mV dec^{-1}. Therefore, it was concluded that the FeO_x loading modification is an effective strategy to improve the OER activity of Ni-foam-based catalysts.

ACKNOWLEDGEMENTS

I would like to share my extreme honor and thank to Professor Elena Baranova, my research supervisor who pictured a great blueprint and presented unlimited guidance for this project during my research period. She gives me such a wonderful opportunity to carry on a research program here and explore the knowledge and mysteries in the field of material synthesis and electrocatalysis.

I would also like to thank the help from the group members of our Laboratory of Electrochemical Engineering (LEE) group. I would not be able to finish my project without their tremendous help. Especially, I would like to show my appreciation to Mohamed S. E. Houache, Antonio D'Orazio and Dr. Evans Monyoncho for their inspiring discussions. Thank you all my fellow lab mates, Emily Cossar, Yasmine Hajar, Raha Einakchi, and Dr. Ebrahim Rezaei, it is you that gave me a lot of good advice and company during the research period.

Thank you to Dr. Marten Ternan and Dr. George Psofogiannakis who taught me how to be a good teaching assistant. All the discussions and corrections that you guys provided are good experiences for me. I would like to thank Dr. Yun Liu for the help and training with the SEM, XRD and EDX characterizations as well as Dr. Nimal Da silva for the help in ICP-AES characterizations.

TABLE OF CONTENTS

LIST OF FIGURES

LIST OF TABLES

LIST OF SYMBOLS

Symbols	Definition	Units
D	Diameter of the crystallite particles	nm
λ	Wavelength of the X-ray source	Å
β	Line broadening at half the maximum intensity	rad
Q	Total electric charge	C

LIST OF ABBREVIATIONS

CA – Chronoamperometry

CE – Counter Electrode

CV – Cyclic voltammetry

DDI – Distilled de-ionized water

ECSA – Electrochemical active surface area

Fe@NMF-O_2/H_2 – FeOx - Nickel meso-foam after O_2/H_2 treatment

Fe@Ni_{DHBT} – FeOx - Dynamic hydrogen bubble templating Ni materials

GCE – Glassy carbon electrode

HER – Hydrogen evolution reaction

Hg/HgO – Mercury mercury oxide

LSV – Linear sweep voltammetry

MP-AES – Microwave plasma - atomic emission spectroscopy

$Ni(Ac)_2$ –Nickel acetate tetrahydrate

NMF – Nickel meso-foam

NMF-H_2 – Nickel meso-foam after direct H_2 treatment

NMF-O_2/H_2 – Nickel meso-foam after O_2/H_2 treatment

Ni_{DHBT} – Dynamic hydrogen bubble templating Ni materials

OER – Oxygen evolution reaction

RE – Reference electrode

SEM – Scanning electron microscopy

TEM – Transmission electron microscopy

WE – Working Electrode

XRD – X-ray diffraction

Chapter 1 - Introduction

1.1 Motivation

The global energy crisis and challenges with environmental pollution have attracted extensive interest and research in the development of efficient and environmentally friendly energy conversion systems, such as water splitting for H_2 production and fuel cells. Water electrolysis is a process of running an electrical current through water, separating hydrogen and oxygen. The hydrogen produced from water electrolysis is a promising clean fuel solution for hydrogen fuel cell vehicles. However, one of the critical reactions that can significantly affect the efficiency of these energy conversion systems is oxygen evolution reaction (OER), for which a rational design of the catalyst is essential. In other words, the practical application of these clean energy techniques requires active and durable OER electrocatalysts.

Nowadays, the best-performing OER catalysts are Ru/Ir-oxides-based materials. However, these catalysts are precious metals. A large scale application of noble metal catalysts in water electrolysis is restricted by the high price of such metals. Therefore, extensive efforts have been devoted to developing low-cost and efficient OER catalysts. The most promising and extensively studied non-precious OER catalysts are transition metal-based materials, which are usually hybrids with carbon materials. The latter not only can work as conductive substrates, but also can provide a large reactive surface area benefiting the electrochemical performance of the catalysts. In addition, it is now well-

recognized that it is the transition metals—especially their oxides, hydroxides, chalcogenide, phosphate, and nitride—that contribute to the promotion of the OER activity.

The rational development of OER catalysts with transition metal components, together with a porous structural design, could further improve the OER performance of the catalysts. The structural design of the catalyst is critical because the OER reactions occur at the gas/catalyst/electrolyte three-phase interface. A porous structure would facilitate the mass transfer process within the catalysts and would therefore benefit their OER activity. Additionally, efficient OER catalysts should not only show high activity, but also exhibit good stability. However, a critical issue in the development of durable OER catalysts is that their oxidative operating potentials would cause oxidation of the electrocatalysts. This issue is more critical for carbon-supported OER catalysts, in which the carbon electrochemical oxidation would lead to the loss or aggregation of carbon-supported transition metal catalysts, and would therefore degrade the durability and electrocatalysis performance.

In summary, previous studies have shown the following: 1) transition metals (e.g. oxides and hydroxides) are efficient OER catalysts in alkaline media; 2) a porous structure design would benefit the overall performance of the catalysts by providing a high surface area, surface area with more active sites and facilities, which helps the diffusion helps the diffusion of the recants and products on the reactive three-phase interface; and 3) the introduction of carbon-based materials might affect the durability performance of OER catalysts. Accordingly, an optimal OER catalyst should be low-cost, have a high surface

area with more active sites, good durability, and a porous structure that facilities mass transportation, because the OER reaction occurs at a solid/liquid electrolyte/gas three-phase interface.

Therefore, in this study, a series of carbon-free porous Ni foam-based OER catalysts have been developed. As-synthesized Ni meso-foam material (raw NMF), with a wire-linked structure and high surface area, was developed. Different heat treatments were performed to modify the NMF surface, such as Ni-meso-foam after direct H_2 treatment (referred to as NMF-H_2) and Ni-meso-foam after O_2 and H_2 treatment (referred to as NMF-O_2/H_2), respectively. The composition, morphology, and electrochemical activity of all materials were studied. In addition to the Ni foam-based materials, a dynamic hydrogen bubble templating Ni materials (referred to as Ni_{DHBT}) OER catalyst was developed synthesized with an electrodeposition and etching method were successfully prepared. The three-dimensional (3D) porous Ni/Zn nanoplatelets were constructed by a two-step gas bubble dynamic template deposition method. The Ni/Zn foil structure was used as a scaffold, which featured an open porous structure and high surface area, for the subsequent electrodeposition of $Ni(OH)_2$. Moreover, to evaluate the effect of the FeO_x deposition toward the OER activity on porous Ni catalysts, the design of Fe loaded NMF-O_2/H_2 materials (referred to as Fe@NMF-O_2/H_2) and Fe loaded Fe@Ni_{DHBT} materials (referred to as Fe@Ni_{DHBT}) were proposed and successfully fabricated.

1.2 Research objectives

Based on the above, the goal of this research is to develop efficient porous Ni based OER electrocatalysts. To achieve this goal, different preparation methods were applied to fabricate a series of Ni materials, and their corresponding OER activity and durability performance were evaluated. The specific objectives of this study are:

i) to develop efficient three dimensional porous Ni foam catalysts, and study the heat treatment effect on the OER performance, e.g. H_2 reduction; O_2 oxidation;

ii) to develop a Ni/$Ni(OH)_2$ layer-structured catalyst using an electrodeposition and etching method, and evaluate its electrochemical performance towards OER;

iii) to develop a series of Fe deposited Ni foam catalysts, and study the effectiveness of Fe component introduction on the catalytic performance of Ni foam catalysts;

iv) to evaluate the physical properties and electrochemical performances of all the synthesized materials listed above, e.g. SEM, XRD MP-AES; CV, CA, LSV and tafel plots;

v) To compare the synthesized materials for OER and recommend the best performing catalyst for future anion exchange membrane water electrolyzer (AEMWE)

1.3 Structure of Thesis

This thesis was consisted of six chapters as follows:

Chapter 1 presents the outline and overview of this thesis, consisting the introduction, motivation and fundamentals of the 3D Ni based OER catalysts. Objectives and contributions of the thesis were also included in this chapter.

Chapter 2 presents an overview and literature reviews on the reported OER catalysts.

In Chapter 3, a facile on pot reflux method in synthesizing 3D porous Ni substrates was introduced, and the synthesis protocol, physical characterizations and electrochemical performances of the NMF materials were discussed.

Chapter 4 shows the schematic synthesis procedure, physical and electrochemical results of another nickel substrate - Ni_{DHBT}s towards OER in alkaline media.

In Chapter 5, a promotion procedure was introduced and adapted in the two substrates synthesized in last two chapters by mixing FeO_x nano particles on the surface pores in further enhancing the catalytic capability towards OER reaction. Meanwhile, physical characterization and electrochemical performances were also investigated.

Chapter 6 presents the conclusions of this study , compare the performance of various materials and give directions in completing and perfecting the future studies of this work.

Chapter 2 — Background and Literature Review

This chapter provides the background to water splitting and the electrocatalysts for hydrogen evolution reaction (HER) and OER. An overview of the topic is presented in the first section. Since OER is considered the limiting step in the overall reaction of for the water splitting, commonly used OER electrocatalysts and their design strategies are reviewed in the second section.

2.1 Overview

Due to increasing concerns over environmental challenges caused by carbon dioxide emissions, extensive efforts have been devoted to the development of renewable and environmentally friendly energy sources and storage devices, such as lithium-ion batteries [1-2], fuel cells [3], water-splitting electrolyzers, and other approaches [4]. H_2 has been considered one of the most ideal clean energy sources of clean energy, and fuel cell systems usually require high purity H_2. Electrocatalytic water splitting is the most promising technology for high purity H_2 production, and therefore, has attracted extensive research interest [5,6].

Electrochemical water splitting involves two crucial half-cell reactions: the cathodic hydrogen evolution reaction and anodic oxygen evolution reaction. Figure 2.1 shows the HER and OER reaction in an alkaline condition. Alkaline water electrolysis is a kind of electrolyzer that has two electrodes operating in an alkaline electrolyte. The electrolyte is usually composed of a potassium hydroxide (KOH) or sodium hydroxide (NaOH) solution. A diaphragm or separator is placed between the two electrodes, separating the product gases and transporting the hydroxide ions (OH^-) between the electrodes.

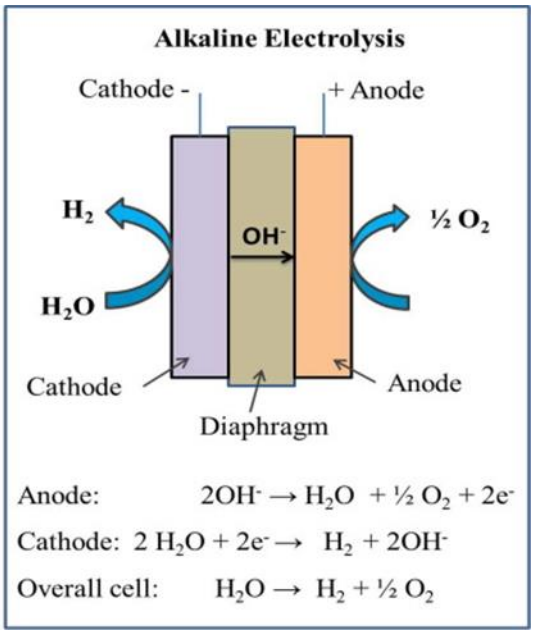

Figure 2.1 Schematic of Alkaline Water Electrolysis

According to the Nernst equation, the theoretical thermodynamic potential for water electrolysis is 1.23 V at 25°C. During water electrolysis, HER and OER are strictly coupled and occur simultaneously. However, compared to that of HER, the reaction kinetics of OER are slow. That is, the overall energy conversion efficiency of water splitting or the H_2 production rate is hindered by the slow OER. Therefore, electrocatalysts that have high

activity and long durability for HER, and for OER in particular, are essential [7].

There are several kinds of existing water electrolysis technologies that can be applied to renewable H_2 energy production, such as high-temperature water electrolysis, alkaline water electrolysis, and proton-exchange membrane water electrolysis. The laws of water electrolysis (discovered and reported from 1833 to 1834) articulate a quantitative relationship between the amount of electricity passing through the electrode/electrolyte interface and the mass of the substances involved in the electrolysis redox process [81].

High-temperature water electrolysis (when the processing is conducted in the solid-oxide cells) is nominated as the SOWE technologies. Solid-oxide electrolysis cells generally operate in the temperature range of 800–1000°C. The most commonly used electrolyte is zirconia (ZrO_2) stabilized with yttrium and scandium oxides [81]. Currently, ceramic membranes are developed and applied in high-temperature water electrolysis. Electrodes are deposited on both surfaces of a thin ceramic membrane that is used as an electrolyte. Even though the SOWE technologies that use solid-oxide cells can be applied in high temperatures on both fuel cells and a water electrolysis mode. However, there are still challenges, such as the electrode corrosion. Due to the time that passes, the degradation processes are further accelerated by the corrosion of the interconnections. In addition, the cell tightness is generally obtained using glass seals or vitro-ceramic seals such that long-term thermal cycling cannot be survived and guaranteed [81].

Alkaline water electrolysis is a simple technology commonly used not only in early 19th century but also today, and it is the main process for the water-splitting processes. For

this process, two metallic electrodes are immersed in a liquid electrolyte, usually high-concentration KOH and NaOH, up to 40wt%, to ensure maximum electrical conductivity at temperatures of up to 90°C. With the development of this technology, more efficient zero-gap cell configurations are applied to lower the interpolar distance and gases at the back of the electrodes by using more porous and pressed electrodes to acquire higher current density values. Alkaline water electrolysis is widely applied in worldwide markets, such as the following: 1) major industrial electric power generator cooling in power plants; 2) semiconductor manufacturing; 3) production units for flat-panel computer and TV displays; 4) heat treatment plants; and 5) analytical chemistry laboratories. From an economic viewpoint, the lifetime of these systems (several tens of thousands of hours of operation) can be considered as satisfactory for continuous operation and are thus profitable. However, current alkaline electrolysis cells can hardly operate at a very low-current density, which is a limit on their great potential in emerging markets. In particular, this is a limit in terms of flexibility in load-following operations, which will be required for the operation of renewable energy sources [81].

Proton-exchange membrane fuel cells, also known as polymer electrolyte membrane (PEM) fuel cells (PEMFC), are a type of fuel cell being developed mainly for transport applications, as well as for stationary fuel-cell applications and portable fuel-cell applications. Their distinguishing features include lower temperature/pressure ranges (50 to 100 ℃) and a special proton-conducting polymer electrolyte membrane. PEMFCs generate electricity and operate on the opposite principle to PEM electrolysis, which

consumes electricity. PEMFCs are built out of membrane electrode assemblies (MEA) which include the electrodes, electrolyte, catalyst, and gas diffusion layers. The MEA is immersed in deionized water. Proton-exchange membrane water electrolysis is an expensive technology; the first electrolyzers were developed for space vehicles and submersibles [81]. There are several advantages to this newly developed applied technology, such as the following: 1) low nominal current density; 2) higher energy consumption; 3) higher delivery current density as well as H_2 delivery pressure and purity; and 4) higher volumetric stack density. Research is still progressing on prolonging the working lifetime of the cells. Some significant advances have been made during the past few years, yet there is still room for further improvement [81].

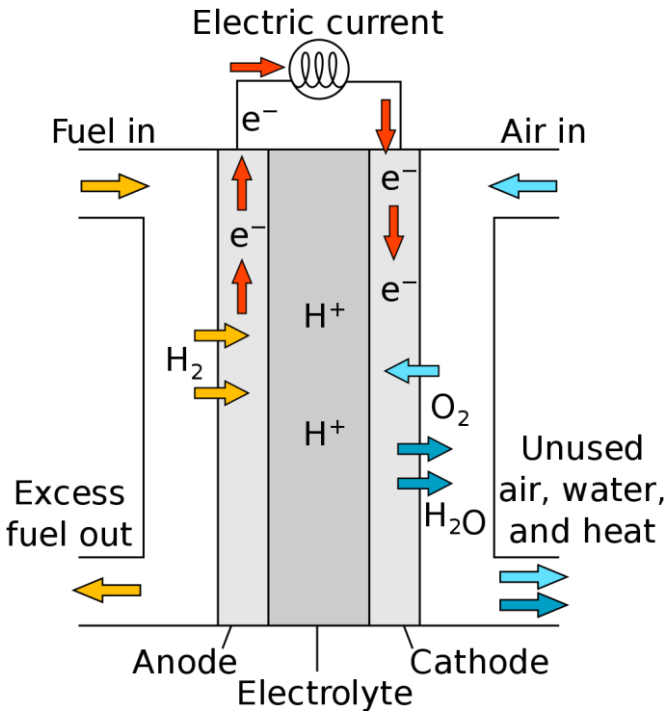

Figure 2.2 Schematic of PEMFC

In recent years, extensive research has been devoted to the development of efficient HER and OER catalysts. The best-performing HER catalysts are Pt-based catalysts and the ideal OER electrocatalysts are noble Ru/Ir oxides [8,9]. However, the high cost of these precious metal catalysts has limited their practical application in water splitting. Recently, the development of anion exchange membrane water electrolysis (AEMWE) technology, which is an alkaline electrolysis process, has attracted much attention. Additionally, it has been reported that AEMWE can operate without expensive noble-metal catalysts [10]. Particularly, transition metal-based metal oxides, hydroxides, sulfides, and their composite materials have been found to exhibit high OER activity in alkaline conditions [11]. Therefore, the development of non-precious water-splitting catalysts especially for OER is crucial for the practical application of AEMWE technology.

2.2 Transition metal based OER catalysts

Recently, transition metals, such as Co, Mn, Ni, Fe, Zn, V and Cu-based materials, have been extensively explored as OER electrocatalysts. Among them, the first-row transition metals, e.g. Ni, Co, and Fe, are the most popular catalysts for OER in alkaline electrolytes. In the following sections, these OER electrocatalysts including their oxides [12-15], hydroxides [16-18], phosphides [19,20], chalcogenides (sulfides, selenides) [21-33], and nitrides [34,35] composites would be briefly reviewed.

2.2.1Co-based OER catalysts

Co-based materials have been regarded as promising alternatives for noble metal-based OER catalysts. The most typical Co-based OER catalyst is Co_3O_4 spinel oxides, which is known having a closed packed array of O^{2-} with Co^{2+} and Co^{3+} cations occupying the tetrahedral and octahedral sites, respectively. Due to its stable spinel structure, Co_3O_4 has been found exhibited both high durability and activity for OER [36]. In addition to Co_3O_4, a comparison study on the OER activity of different cobalt oxides (CoO_x, Co_3O_4, CoO) with similar morphology and nanoparticle sizes, have shown that all these oxides nanoparticles present similar OER activity in alkaline conditions regardless of their oxidation state [37].

This has raised a question on the real Co active site that governs the OER activity. Now, it is well-recognized that the Co^{II} sites would undergo $Co^{II} \rightarrow Co^{III}$ oxidation under OER potential, forming a layered oxidized cobalt species [38,39]. There are also studies reported that higher oxidation state Co^{IV} species can be generated on the outermost surface of the electrode [38,40]. That is, the OER catalytic site on the oxides electrode is the in-situ formed quasi-reversible redox couple Co^{III}/Co^{IV} species during OER reaction [41-44].

In fact, in addition to the cobalt oxides, its hydroxide, chalcogenides (sulfides, selenides), nitrides, phosphide, etc. has also shown excellent OER activity [45-51]. Also, by using strategies, such as heteroatom doping and porous structure design, the OER activity of these catalysts can be further improved [52]. For example, Dai et al. [53] developed a high performance OER catalyst by using ammonia treatment to etch and dope N in the cobalt sulfides-graphene hybrid. Zou et al. [54] found that the introduction of Zn to synthesize a

bimetallic ZnCo layered double hydroxide would result in a much lower OER overpotential, by ~100 mV, than that of $Co(OH)_2$ and Co_3O_4. In addition, Wang et al [55] reported that, by embedding Co nanoparticles into the porous carbon material, the OER activity and stability of the hybrid catalysts can be greatly enhanced.

It is also reported that doping Cu metal would alter the electrical conductivity of cobalt phosphide, and therefore enhance the activity for OER. For example, Song et al. [56] have observed that $Cu_{0.3}Co_{2.7}P$ supported on N doped carbon materials exhibit remarkably high activity for OER. Xiong et al. [57] reported that incorporating MnO_2 with cobalt phosphides, MnO_2-CoP_3, can also improve the stability and activity for OER. The introduction of Mo into cobalt chalcogenides is also beneficial for OER activity. Sun et al. [58] fabricated an amorphous defect-rich $CoMoS_4$ via a one-step hydrothermal method, and have observed that $CoMoS_4$ exhibit high durability and activity for OER under alkaline conditions. Noted that, although showing higher OER activity, under the oxidizing condition of OER, metal phosphide and chalcogenides are thermodynamically less stable than oxides. This suggests that these cobalt phosphide and chalcogenides might not be the real active components catalyzing OER reaction. Recent synchrotron radiation X-ray absorption and in-situ Raman spectroscopy analysis have shown that, during OER, there is a dynamic conversion between Co_3O_4, $Co(OH)_2$ and CoO(OH) species [59].

2.2.2Ni-based OER electrocatalysts

Ni is also a first-row transition element, and has also attracted extensive attention in

water splitting eletrocatalysis. It is an earth-abundant material and cheaper than Co. Similar with cobalt, nickel oxides also show good activity for OER in alkaline condition. A typical strategy to boost the catalytic activity of nickel oxides is to optimize the nanostructured morphology with large active surface area [60]. For example, Zhang et al. [61] reported that ultrafine NiO nanosheets with a platelet size around 4.0 nm and thickness of ~ 1.1 nm stabilized by TiO_2 exhibits very high OER activity.

Recently, many studies have shown that the valence state of surface Ni would also undergo oxidation during OER reaction, and it is the Ni site with higher valence state that contributes to the OER activity. Thus, various approaches to prepare nickel oxides with higher valence state have been proposed to improve the catalytic performance [62]. Cation doping is another strategy to improve the catalytic performance of nickel oxide [63]. For example, Jaramillo et al. [64] demonstrated the introduction of Ce dopant would significantly enhance the OER activity of electrodeposited NiO_x films.

In addition to nickel oxides, nickel oxyhydroxide have also been extensively investigated in OER catalysis, and the strategies mentioned above also apply to the design of efficient nickel-based oxyhydroxide catalysts. For example, Boettcher and co-workers [65] demonstrated that heteroatomic Fe-doping in nickel-based oxyhydroxide (Fe-NiO_xH_y) can be a promising method to improve the OER activity. The beneficial effect of Fe doping has been explained by the local coordination structure in Fe-NiO_xH_y [66]. Moreover, instead of directly doping heteroatoms, Stahl et al. [67] reported an in-situ dissolve method to fabricate efficient nickel hydroxides OER catalysts. In that study, an inverse spinel

$NiFeAlO_4$ material was developed. During the water electrolysis, the Al atom will partially dissolve into the alkaline electrolyte, leading to the in-situ formation of porous nickel hydroxides as the active OER catalysts layer. The latter shows significantly improved OER activity than that of NiO, NiFe and $NiFe_2O_4$.

Recently, Ni nitrides, phosphide and chalcogenides were also found exhibit excellent OER activity. For example, Zhang et al. [68] developed porous bimetallic iron–nickel nitride ($FeNi_3N$) nanorods, which exhibit remarkably high activity and stability for OER. Zheng et al. [69] have observed that nanostructured hexagonal Ni_2P exhibit a high activity for OER. Liu et al. [70] prepared a Zn doped Ni_3S_2 (Zn-Ni_3S_2) nanosheet by hydrothermal reaction. The Zn-Ni_3S_2 with high electrochemically active surface area was found exhibited excellent activity for OER. That study concluded that doping Zn with Ni_3S_2 enhance the durability and activity for OER. In another study, Hu et al. [71] reported an efficient NiSe OER catalyst and found NiSe was completely converted into $Ni(OH)_2$ crystal after OER reaction under alkaline conditions. The hydroxide component was claimed as the real OER catalyst in Ni chalcogenides.

2.2.3Fe-based OER electrocatalysts

Fe is the most abundant transition element on earth, which is also much cheaper and less toxic compared with Co and Ni. Usually, the Fe oxides or hydroxide materials were hybrid with other transition metals to obtain high OER activities. For example, many studies have reported that bimetallic iron–nickel oxyhydroxide can significantly enhance

OER activity. For example, Ye et al. [72] reported that NiFeOOH supported on graphite sheet exhibits excellent stability and activity for OER. Li et al. [73] found that, the increased OER activity of NiFe layered double hydroxide (NiFe-LDH) might be resulted from increased inter-layer spacing of the two-dimensional hydroxide. In another study, Yu et al. [74] have observed that depositing NiFe LDH on nanostructured Cu can enhance the surface area, and improve its activity for OER. Gao et al. [75] found that addition of V to Co-Fe oxide would result in to improved OER activity than that of $(CoFe_2)O_4$ and $Co_3V_2O_8$.

Meanwhile, proper structural design of the Fe-based catalysts is also effective in improving their OER activities. For example, Zhao et al. [76] developed a nanoarchitectured composite material, which consist of Fe_3C nanoparticles encapsulated at the tip of nitrogen-enriched carbon nanotubes (NCNTs). The NCNTs were aligned on nitrogen-doped carbon nanofibers, forming a 3D structured Fe_3C@NCNTs-NCNFs catalyst. This endows the unique 3D hierarchical architecture of Fe_3C@NCNTs-NCNFs with highly exposed active sites, enhanced electrons transfer properties and strong synergistic effects. Due to these beneficial features, a high OER activity is achieved by Fe_3C@NCNTs-NCNFs. In another study, Ma et al. [77] fabricated a hollow structured FeNi/$NiFe_2O_4$@NC materials, which also delivers enhance high durability and activity for OER. Li et al. [78] developed a nanostructured Fe-doped Ni_2P catalyst, $(Ni_{0.33}Fe_{0.67})_2P$, which also shows remarkably enhanced OER activity. In addition, porous Fe-based OER catalysts derived from bimetal metal organic frameworks (MOFs) materials are also reported. [79] The redox-active metals and organic linkers in MOFs can serve as both redox and proton transfer mediator, which

can enhance the durability and activity for OER. [80]

2.3 Summary

A major obstacle that hinders the practical application of water electrolysis technology for the production of clean hydrogen sources is the development of low-cost, high-efficient, and earth-abundant electrocatalysts catalyzing the HER and OER electrochemical reactions. The OER reaction is more critical, because it usually exhibits much slower reaction kinetics than HER. Therefore, it is highly desirable to prepare low-cost catalysts with high efficiency to catalyze the OER in water splitting. Due to their earth-abundant nature and good catalytic activity, transition metal-based materials, such as oxides/hydroxides, are promising OER catalysts. In particular, for the Ni and Fe based transition metals, they are relatively cheap and usually exhibit excellent ORR activity. Therefore, the design of efficient and durable non-precious OER catalysts for water electrolysis should include: *i)* a careful selection of electronic conductive and low-cost active transition metal materials; *ii)* a rational morphology design and elaborately tuned architecture that have active sites with the enlarged mass transfer efficiency, e.g. introducing mesoporous materials and 3D architectures; and *iii)* maximizing the synergistic effects of hybridizing catalysts.

References

[1]. Lewis, N. S., & Nocera, D. G. (1958). National academy of sciences. *Endocrinology*, *63*(5), 707.

[2]. Hunter, B. M., Gray, H. B., & Müller, A. M. (2016). Earth-Abundant Heterogeneous Water Oxidation Catalysts. *Chemical Reviews*, *116*(22), 14120–14136.

[3]. You, B., & Sun, Y. (2016). Chalcogenide and Phosphide Solid-State Electrocatalysts for Hydrogen Generation. *ChemPlusChem*, *81*(10), 1045–1055.

[4]. Jiao, Y., Zheng, Y., Jaroniec, M., & Qiao, S. Z. (2015). Design of electrocatalysts for oxygen- and hydrogen-involving energy conversion reactions. *Chemical Society Reviews*, *44*(8), 2060–2086.

[5]. Zhu, Y. P., Guo, C., Zheng, Y., & Qiao, S. Z. (2017). Surface and Interface Engineering of Noble-Metal-Free Electrocatalysts for Efficient Energy Conversion Processes. *Accounts of Chemical Research*, *50*(4), 915–923.

[6]. Li, X., Hu, X. L., Wang, X. L., Pan, Q. Q., Liu, L., & Su, Z. M. (2019). A substrate-free Mo_2C-based electrocatalyst by facile glucose-blowing for efficient hydrogen production. *New Journal of Chemistry*, *43*(48), 18970–18974.

[7]. Li, X., Hao, X., Abudula, A., & Guan, G. (2016). Nanostructured catalysts for electrochemical water splitting: Current state and prospects. *Journal of Materials Chemistry A*, *4*(31), 11973–12000.

[8]. Durst, J., Siebel, A., Simon, C., Hasché, F., Herranz, J., & Gasteiger, H. A. (2014). New insights into the electrochemical hydrogen oxidation and evolution reaction

mechanism. *Energy and Environmental Science*, *7*(7), 2255–2260.

[9]. Shan, J., Guo, C., Zhu, Y., Chen, S., Song, L., Jaroniec, M., Zheng, Y., & Qiao, S. Z. (2019). Charge-Redistribution-Enhanced Nanocrystalline Ru@IrOx Electrocatalysts for Oxygen Evolution in Acidic Media. *Chem*, *5*(2), 445–459.

[10]. E.Cossar, A.O.Barnett, F.Seland, & E.A.Baranova. (2019). The Performance of Nickel and Nickel-Iron Catalysts Water Electrolysis. *Catalysts*.

[11]. Liu, Y., Jiang, H., Zhu, Y., Yang, X., & Li, C. (2016). Transition metals (Fe, Co, and Ni) encapsulated in nitrogen-doped carbon nanotubes as bi-functional catalysts for oxygen electrode reactions. *Journal of Materials Chemistry A*, *4*(5), 1694–1701.

[12]. Zhu, X., Wang, P., Wang, Z., Liu, Y., Zheng, Z., Zhang, Q., Zhang, X., Dai, Y., Whangbo, M. H., & Huang, B. (2018). Co_3O_4 nanobelt arrays assembled with ultrathin nanosheets as highly efficient and stable electrocatalysts for the chlorine evolution reaction. *Journal of Materials Chemistry A*, *6*(26), 12718–12723.

[13]. Du, J., Chen, C., Cheng, F., & Chen, J. (2015). Rapid synthesis and efficient electrocatalytic oxygen reduction/evolution reaction of $CoMn_2O_4$ nanodots supported on graphene. *Inorganic Chemistry*, *54*(11), 5467–5474.

[14]. Lu, X. F., Gu, L. F., Wang, J. W., Wu, J. X., Liao, P. Q., & Li, G. R. (2017). Bimetal-Organic Framework Derived $CoFe_2O_4$/C Porous Hybrid Nanorod Arrays as High-Performance Electrocatalysts for Oxygen Evolution Reaction. *Advanced Materials*, *29*(3).

[15]. Merrill, M. D., & Dougherty, R. C. (2008). Metal oxide catalysts for the evolution of

O_2 from H_2O. *Journal of Physical Chemistry C*, *112*(10), 3655–3666.

[16]. Song, F., & Hu, X. (2014). Ultrathin cobalt-manganese layered double hydroxide is an efficient oxygen evolution catalyst. *Journal of the American Chemical Society*, *136*(47), 16481–16484.

[17]. Ping, J., Wang, Y., Lu, Q., Chen, B., Chen, J., Huang, Y., Ma, Q., Tan, C., Yang, J., Cao, X., Wang, Z., Wu, J., Ying, Y., & Zhang, H. (2016). Self-Assembly of Single-Layer CoAl-Layered Double Hydroxide Nanosheets on 3D Graphene Network Used as Highly Efficient Electrocatalyst for Oxygen Evolution Reaction. *Advanced Materials*, *28*(35), 7640–7645.

[18]. Hunter, B. M., Hieringer, W., Winkler, J. R., Gray, H. B., & Müller, A. M. (2016). Effect of interlayer anions on [NiFe]-LDH nanosheet water oxidation activity. *Energy and Environmental Science*, *9*(5), 1734–1743.

[19]. Wang, Y., Williams, T., Gengenbach, T., Kong, B., Zhao, D., Wang, H., & Selomulya, C. (2017). Unique hybrid $Ni_2P/MoO_2@MoS_2$ nanomaterials as bifunctional non-noble-metal electro-catalysts for water splitting. *Nanoscale*, *9*(44), 17349–17356.

[20]. Li, J., Yan, M., Zhou, X., Huang, Z. Q., Xia, Z., Chang, C. R., Ma, Y., & Qu, Y. (2016). Mechanistic Insights on Ternary Ni_2−xCoxP for Hydrogen Evolution and Their Hybrids with Graphene as Highly Efficient and Robust Catalysts for Overall Water Splitting. *Advanced Functional Materials*, *26*(37), 6785–6796.

[21]. Xue, Y., Ren, Z., Xie, Y., Du, S., Wu, J., Meng, H., & Fu, H. (2017). CoSe:X

nanocrystalline-dotted CoCo layered double hydroxide nanosheets: A synergetic engineering process for enhanced electrocatalytic water oxidation. *Nanoscale*, *9*(42), 16256–16263.

[22]. Liu, Y., Xiao, C., Lyu, M., Lin, Y., Cai, W., Huang, P., Tong, W., Zou, Y., & Xie, Y. (2015). Ultrathin Co3S4Nanosheets that Synergistically Engineer Spin States and Exposed Polyhedra that Promote Water Oxidation under Neutral Conditions. *Angewandte Chemie - International Edition*, *54*(38), 11231–11235.

[23]. Fu, X. X., Kang, X. N., Zhang, B., Xiong, C., Jiang, X. Z., Xu, D. S., Du, W. M., & Zhang, G. Y. (2011). Light transmission from the large-area highly ordered epoxy conical pillar arrays and application to GaN-based light emitting diodes. *Journal of Materials Chemistry*, *21*(26), 9576–9581.

[24]. Gao, M. R., Gao, Q., Jiang, J., Cui, C. H., Yao, W. T., & Yu, S. H. (2011). A methanol-tolerant Pt/$CoSe_2$ nanobelt cathode catalyst for direct methanol fuel cells. *Angewandte Chemie - International Edition*, *50*(21), 4905–4908.

[25]. Zhang, H., Lei, L., & Zhang, X. (2014). One-step synthesis of cubic pyrite-type $CoSe_2$ at low temperature for efficient hydrogen evolution reaction. *RSC Advances*, *4*(97), 54344–54348.

[26]. Yu, X., Sun, W., & Chu, Y. (2014). One-pot solvothermal synthesis and properties of 1D NiSe and NiSe-Ni_3S_2 alloyed compound nanorod arrays. *New Journal of Chemistry*, *38*(1), 70–76.

[27]. Chen, Z., Higgins, D., Yu, A., Zhang, L., & Zhang, J. (2011). A review on non-

precious metal electrocatalysts for PEM fuel cells. *Energy and Environmental Science*, *4*(9), 3167–3192.

[28]. Zhu, L., Susac, D., Teo, M., Wong, K. C., Wong, P. C., Parsons, R. R., Bizzotto, D., Mitchell, K. A. R., & Campbell, S. A. (2008). Investigation of CoS_2-based thin films as model catalysts for the oxygen reduction reaction. *Journal of Catalysis*, *258*(1), 235–242.

[29]. Zhou, Y. X., Yao, H. Bin, Wang, Y., Liu, H. L., Gao, M. R., Shen, P. K., & Yu, S. H. (2010). Hierarchical hollow Co_9S_8 microspheres: Solvothermal synthesis, magnetic, electrochemical, and electrocatalytic properties. *Chemistry - A European Journal*, *16*(39), 12000–12007.

[30]. He, Ting & Alonso-Vante, Nicolas. (2008). In situ Free-Surfactant Synthesis and ORR-Electrochemistry of Carbon-Supported Co_3S_4 and $CoSe_2$ Nanoparticles. Chem. Mater. 20. 26-28.

[31]. Vayner, E., Sidik, R. A., Anderson, A. B., & Popov, B. N. (2007). Experimental and theoretical study of cobalt selenide as a catalyst for O_2 electroreduction. *Journal of Physical Chemistry C*, *111*(28), 10508–10513.

[32]. Feng, Y., He, T., & Alonso-Vante, N. (2009). Oxygen reduction reaction on carbon-supported $CoSe_2$ nanoparticles in an acidic medium. *Electrochimica Acta*, *54*(22), 5252–5256.

[33]. Wu, G., Cui, G., Li, D., Shen, P. K., & Li, N. (2009). Carbon-supported $Co_{1.67}Te_2$ nanoparticles as electrocatalysts for oxygen reduction reaction in alkaline electrolyte.

Journal of Materials Chemistry, *19*(36), 6581–6589.

[34]. Jia, X., Zhao, Y., Chen, G., Shang, L., Shi, R., Kang, X., Waterhouse, G.I.N., Wu, L.-Z., Tung, C.-H. and Zhang, T. (2016), Water Splitting: Ni_3FeN Nanoparticles Derived from Ultrathin NiFe-Layered Double Hydroxide Nanosheets: An Efficient Overall Water Splitting Electrocatalyst. Adv. Energy Mater., 6, 1502585.

[35]. Lee, K. J., Shin, D. Y., Byeon, A., Lim, A., Jo, Y. S., Begley, A., Lim, D. H., Sung, Y. E., Park, H. S., Chae, K. H., Nam, S. W., Lee, K. Y., & Kim, J. Y. (2017). Hierarchical cobalt-nitride and -oxide co-doped porous carbon nanostructures for highly efficient and durable bifunctional oxygen reaction electrocatalysts. *Nanoscale*, *9*(41), 15846–15855.

[36]. Esswein, A. J., Surendranath, Y., Reece, S. Y., & Nocera, D. G. (2011). Highly active cobalt phosphate and borate based oxygen evolving catalysts operating in neutral and natural waters. *Energy and Environmental Science*, *4*(2), 499–504.

[37]. Chou, N. H., Ross, P. N., Bell, A. T., & Tilley, T. D. (2011). Comparison of cobalt-based nanoparticles as electrocatalysts for water oxidation. *ChemSusChem*, *4*(11), 1566–1569.

[38]. Lyons, M. E. G., & Brandon, M. P. (2008). The oxygen evolution reaction on passive oxide covered transition metal electrodes in alkaline solution part ii - cobalt. *International Journal of Electrochemical Science*, *3*(12), 1425–1462.

[39]. Yeo, B. S., & Bell, A. T. (2011). Enhanced activity of gold-supported cobalt oxide for the electrochemical evolution of oxygen. *Journal of the American Chemical*

Society, *133*(14), 5587–5593.

[40]. Simmons, G. W. (1976). In Situ Studies of the Passivation and Anodic Oxidation of Cobalt by Emission Mössbauer Spectroscopy. *Journal of The Electrochemical Society*, *123*(9), 1276.

[41]. Mattioli, G., Giannozzi, P., Amore Bonapasta, A., & Guidoni, L. (2013). Reaction pathways for oxygen evolution promoted by cobalt catalyst. *Journal of the American Chemical Society*, *135*(41), 15353–15363.

[42]. Bajdich, M., García-Mota, M., Vojvodic, A., Nørskov, J. K., & Bell, A. T. (2013). Theoretical investigation of the activity of cobalt oxides for the electrochemical oxidation of water. *Journal of the American Chemical Society*, *135*(36), 13521–13530.

[43]. Liu, J., Liu, Y., Liu, N., Han, Y., Zhang, X., Huang, H., Lifshitz, Y., Lee, S. T., Zhong, J., & Kang, Z. (2015). Metal-free efficient photocatalyst for stable visible water splitting via a two-electron pathway. *Science*, *347*(6225), 970–974.

[44]. Barkaoui, S., Haddaoui, M., Dhaouadi, H., Raouafi, N., & Touati, F. (2015). Hydrothermal synthesis of urchin-like Co_3O_4 nanostructures and their electrochemical sensing performance of H_2O_2. *Journal of Solid State Chemistry*, *228*(2015), 226–231.

[45]. Ma, T. Y., Dai, S., Jaroniec, M., & Qiao, S. Z. (2014). Metal-organic framework derived hybrid Co_3O_4-carbon porous nanowire arrays as reversible oxygen evolution electrodes. *Journal of the American Chemical Society*, *136*(39), 13925–13931.

[46]. Zhu, Y.-P., Liu, Y.-P., Ren, T.-Z. and Yuan, Z.-Y. (2015), Self-Supported Cobalt Phosphide Mesoporous Nanorod Arrays: A Flexible and Bifunctional Electrode for Highly Active Electrocatalytic Water Reduction and Oxidation. Adv. Funct. Mater., 25: 7337-7347.

[47]. Jin, Z., Li, P., & Xiao, D. (2016). Metallic Co_2P ultrathin nanowires distinguished from CoP as robust electrocatalysts for overall water-splitting. *Green Chemistry*, *18*(6), 1459–1464.

[48]. Yang, Y., Fei, H., Ruan, G., & Tour, J. M. (2015). Porous cobalt-based thin film as a bifunctional catalyst for hydrogen generation and oxygen generation. *Advanced Materials*, *27*(20), 3175–3180.

[49]. Ryu, J., Jung, N., Jang, J. H., Kim, H. J., & Yoo, S. J. (2015). In Situ Transformation of Hydrogen-Evolving CoP Nanoparticles: Toward Efficient Oxygen Evolution Catalysts Bearing Dispersed Morphologies with Co-oxo/hydroxo Molecular Units. *ACS Catalysis*, *5*(7), 4066–4074.

[50]. Chang, J., Xiao, Y., Xiao, M., Ge, J., Liu, C., & Xing, W. (2015). Surface Oxidized Cobalt-Phosphide Nanorods As an Advanced Oxygen Evolution Catalyst in Alkaline Solution. *ACS Catalysis*, *5*(11), 6874–6878.

[51]. Wang, P., Song, F., Amal, R., Ng, Y. H., & Hu, X. (2016). Efficient Water Splitting Catalyzed by Cobalt Phosphide-Based Nanoneedle Arrays Supported on Carbon Cloth. *ChemSusChem*, *9*(5), 472–477.

[52]. Cui, L., Qu, F., Liu, J., Du, G., Asiri, A. M., & Sun, X. (2017). Interconnected

Network of Core–Shell CoP@CoBiPi for Efficient Water Oxidation Electrocatalysis under Near Neutral Conditions. *ChemSusChem*, *10*(7), 1370–1374.

[53]. Dou, S., Tao, L., Huo, J., Wang, S., & Dai, L. (2016). Etched and doped Co_9S_8/graphene hybrid for oxygen electrocatalysis. *Energy and Environmental Science*, *9*(4), 1320–1326.

[54]. Zou, X., Goswami, A., & Asefa, T. (2013). Efficient noble metal-free (electro)catalysis of water and alcohol oxidations by zinc-cobalt layered double hydroxide. *Journal of the American Chemical Society*, *135*(46), 17242–17245.

[55]. Kanan, M. W., Surendranath, Y., & Nocera, D. G. (2009). Cobalt-phosphate oxygen-evolving compound. *Chemical Society Reviews*, *38*(1), 109–114.

[56]. Song, J., Zhu, C., Xu, B.Z., Fu, S., Engelhard, M.H., Ye, R., Du, D., Beckman, S.P. and Lin, Y. (2017), Water Splitting: Bimetallic Cobalt-Based Phosphide Zeolitic Imidazolate Framework: CoP_x Phase-Dependent Electrical Conductivity and Hydrogen Atom Adsorption Energy for Efficient Overall Water Splitting (Adv. Energy Mater. 2/2017). Adv. Energy Mater., 7 1601555

[57]. Xiong, X., Ji, Y., Xie, M., You, C., Yang, L., Liu, Z., Asiri, A. M., & Sun, X. (2018). MnO_2-CoP_3 nanowires array: An efficient electrocatalyst for alkaline oxygen evolution reaction with enhanced activity. *Electrochemistry Communications*, *86*(December 2017), 161–165.

[58]. Sun, Y., Wang, C., Ding, T., Zuo, J., & Yang, Q. (2016). Fabrication of amorphous $CoMoS_4$ as a bifunctional electrocatalyst for water splitting under strong alkaline

conditions. *Nanoscale*, *8*(45), 18887–18892.

[59]. Yoon, T. and Kim, K.S. (2016), Water Splitting: One-Step Synthesis of CoS-Doped β-$Co(OH)_2$@Amorphous MoS_{2+x} Hybrid Catalyst Grown on Nickel Foam for High-Performance Electrochemical Overall Water Splitting. Adv. Funct. Mater., 26: 7386-7393.

[60]. Tahir, M., Pan, L., Idrees, F., Zhang, X., Wang, L., Zou, J. J., & Wang, Z. L. (2017). Electrocatalytic oxygen evolution reaction for energy conversion and storage: A comprehensive review. *Nano Energy*, *37*(May), 136–157.

[61]. Zhao, Y., Jia, X., Chen, G., Shang, L., Waterhouse, G. I. N., Wu, L. Z., Tung, C. H., Ohare, D., & Zhang, T. (2016). Ultrafine NiO Nanosheets Stabilized by TiO_2 from Monolayer NiTi-LDH Precursors: An Active Water Oxidation Electrocatalyst. *Journal of the American Chemical Society*, *138*(20), 6517–6524.

[62]. Zheng, X., Zhang, B., De Luna, P., Liang, Y., Comin, R., Voznyy, O., Han, L., Garc á De Arquer, F. P., Liu, M., Dinh, C. T., Regier, T., Dynes, J. J., He, S., Xin, H. L., Peng, H., Prendergast, D., Du, X., & Sargent, E. H. (2018). Theory-driven design of high-valence metal sites for water oxidation confirmed using in situ soft X-ray absorption. *Nature Chemistry*, *10*(2), 149–154.

[63]. Li, B., Chen, S., Tian, J., Gong, M., Xu, H., & Song, L. (2017). Amorphous nickel-iron oxides/carbon nanohybrids for an efficient and durable oxygen evolution reaction. *Nano Research*, *10*(11), 3629–3637.

[64]. J. W. D. Ng, M. Garc á-Melchor, M. Bajdich, P. Chakthranont, C. Kirk, A. Vojvodic,

T. F. Jaramillo. (2016) Gold-supported cerium-doped NiO_x catalysts for water oxidation, Nat. Energy 1, 16053.

[65]. Trotochaud, L., Young, S. L., Ranney, J. K., & Boettcher, S. W. (2014). Nickel-Iron oxyhydroxide oxygen-evolution electrocatalysts: The role of intentional and incidental iron incorporation. *Journal of the American Chemical Society*, *136*(18), 6744–6753.

[66]. Stevens, M. B., Trang, C. D. M., Enman, L. J., Deng, J., & Boettcher, S. W. (2017). Reactive Fe-Sites in Ni/Fe (Oxy)hydroxide Are Responsible for Exceptional Oxygen Electrocatalysis Activity. *Journal of the American Chemical Society*, *139*(33), 11361–11364.

[67]. Chen, J. Y. C., Miller, J. T., Gerken, J. B., & Stahl, S. S. (2014). Inverse spinel $NiFeAlO_4$ as a highly active oxygen evolution electrocatalyst: Promotion of activity by a redox-inert metal ion. *Energy and Environmental Science*, *7*(4), 1382–1386.

[68]. Zhang, B., Xiao, C., Xie, S., Liang, J., Chen, X., & Tang, Y. (2016). Iron-nickel nitride nanostructures in situ grown on surface-redox-etching nickel foam: Efficient and ultrasustainable electrocatalysts for overall water splitting. *Chemistry of Materials*, *28*(19), 6934–6941.

[69]. Zheng, J., Zhou, W., Liu, T., Liu, S., Wang, C., & Guo, L. (2017). Homologous NiO//Ni_2P nanoarrays grown on nickel foams: a well matched electrode pair with high stability in overall water splitting. *Nanoscale*, *9*(13), 4409–4418.

[70]. Liu, X., Chang, Z., Luo, L., Xu, T., Lei, X., Liu, J., & Sun, X. (2014). Hierarchical

Zn x $Co_{3-x}O_4$ nanoarrays with high activity for electrocatalytic oxygen evolution. *Chemistry of Materials*, *26*(5), 1889–1895.

[71]. Xu, X., Song, F., & Hu, X. (2016). A nickel iron diselenide-derived efficient oxygen-evolution catalyst. *Nature Communications*, *7*, 1–7.

[72]. Ye, Y. J., Zhang, N., & Liu, X. X. (2017). Amorphous NiFe(oxy)hydroxide nanosheet integrated partially exfoliated graphite foil for high efficiency oxygen evolution reaction. *Journal of Materials Chemistry A*, *5*(46), 24208–24216.

[73]. Li, X., Hao, X., Wang, Z., Abudula, A., & Guan, G. (2017). In-situ intercalation of NiFe LDH materials: An efficient approach to improve electrocatalytic activity and stability for water splitting. *Journal of Power Sources*, *347*, 193–200.

[74]. Yu, L., Zhou, H., Sun, J., Qin, F., Yu, F., Bao, J., Yu, Y., Chen, S., & Ren, Z. (2017). Cu nanowires shelled with NiFe layered double hydroxide nanosheets as bifunctional electrocatalysts for overall water splitting. *Energy and Environmental Science*, *10*(8), 1820–1827.

[75]. Gao, T., Jin, Z., Liao, M., Xiao, J., Yuan, H., & Xiao, D. (2015). A trimetallic V-Co-Fe oxide nanoparticle as an efficient and stable electrocatalyst for oxygen evolution reaction. *Journal of Materials Chemistry A*, *3*(34), 17763–17770.

[76]. Zhao, Y., Zhang, J., Guo, X., Fan, H., Wu, W., Liu, H., & Wang, G. (2017). Fe_3C@nitrogen doped CNT arrays aligned on nitrogen functionalized carbon nanofibers as highly efficient catalysts for the oxygen evolution reaction. *Journal of Materials Chemistry A*, *5*(37), 19672–19679.

[77]. Ma, Y., Dai, X., Liu, M., Yong, J., Qiao, H., Jin, A., Li, Z., Huang, X., Wang, H., & Zhang, X. (2016). Strongly Coupled FeNi Alloys/$NiFe_2O_4$@Carbonitride Layers-Assembled Microboxes for Enhanced Oxygen Evolution Reaction. *ACS Applied Materials and Interfaces*, *8*(50), 34396–34404.

[78]. Li, Y., Zhang, H., Jiang, M., Zhang, Q., He, P., & Sun, X. (2017). 3D Self-Supported Fe-Doped Ni_2P Nanosheet Arrays as Bifunctional Catalysts for Overall Water Splitting. *Advanced Functional Materials*, *27*(37), 1–8.

[79]. Le Formal, F. L.; Guijarro, N.; Bourée, W. S.; Gopakumar, A.; Prévot, M. S.; Daubry, A.; Lombardo, L.; Sornay, C.; Voit, J.; Magrez, A.; Dyson P.J.; Sivula K. (2016) Formation of Efficient Water Oxidation Electrocatalyst on Gibeon Meteorite and Stainless Steel Electrodes. Energy Environ. Sci. *9*, 3448-3455.

[80]. Zhang, X., Liu, Q., Shi, X., Asiri, A. M., & Sun, X. (2018). An Fe-MOF nanosheet array with superior activity towards the alkaline oxygen evolution reaction. Inorganic Chemistry Frontiers, 5(6), 1405–1408.

[81]. Millet, P., & Grigoriev, S. (2013). Water Electrolysis Technologies. Renewable Hydrogen Technologies: Production, Purification, Storage, Applications and Safety, 19–41.

Chapter 3 — Ni meso-foams for OER reaction

In this chapter, a series of three-dimensional structured porous Ni foam catalysts were developed. The surface of these catalysts was modified through different heat treatment method, e.g. under H_2 reduction or O_2 oxidation. The OER activity and stability of these catalysts were evaluated. The results show that the Ni foam obtained by successive O_2 oxidation and H_2 reduction treatment possesses the best OER activity (overpotential of ~ 364 mV at 10 mA/cm^2), and exhibits good stability as well.

3.1 Introduction

Due to their good electrochemical activity and low cost, nickel-based materials are of great significance in energy storage and conversion applications, e.g. water splitting [1, 2]. Meanwhile, previous studies have demonstrated that, in addition to the intrinsic catalytic properties of the materials, micro-porous design of the catalysts also plays an important role in improving its OER activity: the micro-porous structure not only provides an increased surface area for the active sites, but also facilities the mass transportation at the gas/solid/electrolyte three-phase interface, at which the OER reaction occurs [3-5]. Accordingly, the development of hierarchical nanostructured nickel OER catalysts assembled by dimensional porous building nanoparticles has attracted many attentions [6].

For the fabrication of Ni micro-/nanostructures, various physical and chemical

methods have been reported in the literature [7,8]. For example, using a hydrothermal route, Zhu et al. [7] developed a self-assembled three-dimensional (3D) flower-like hierarchical $Ni(OH)_2$ hollow architecture. Qiao et al. [9] reported a mesoporous three-dimensional flowerlike NiO material through a template-free modified homogeneous precipitation method. Moreover, among these dimensional Ni nanostructures, the 3D nanostructured catalysts usually have substantially increased electroactive surface area than low dimensional materials, and therefore may provide enhanced catalytic activity [10].

Thus, in the present study, a series of 3D structured porous Ni foam-based OER catalysts were fabricated using a facile one-pot reflux method. In fact, each reported method for synthesizing 3D materials has its own advantages. The one-pot reflux method is chosen in this study become of its simple and surfactant-free process. In addition, upon the successful preparation of 3D Ni foam catalysts, different heat treatment procedures, e.g. H_2 reduction or O_2 oxidation, were introduced to modify their surface state. The activity and stability of these 3D Ni foam catalysts towards OER were evaluated in 1M KOH. The results show that the Ni foam obtained by O_2 oxidation H2 reduction, referred to as NMF-O2/H2, possesses the best performance for OER reaction: when a current density of 10 mA/cm2 is generated, it has an overpotential of ~ 364 mV under 25 ℃. All the electrochemical results were referred to the Hg/HgO as the reference electrode.

3.2 Experimental Procedure

3.2.1Synthesis of Ni meso-foam (NMF)

A low-density nickel meso-foam with high porosity was synthesized through a facile one-pot reflux method by using nickel acetate tetrahydrate ($Ni(Ac)_2$) (99.998%, Sigma-Aldrich) as precursor and glycerol (≥99.5%, Fisher Scientific) as the reducing agent.[11-14]

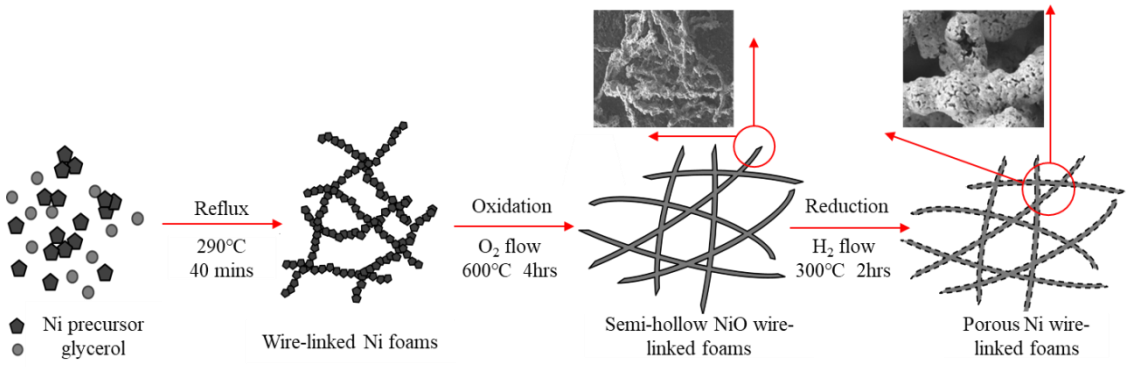

Fig 3.1 Schematic for the synthesis procedure of NMF

In a typical synthesis procedure, 0.9996mg $Ni(Ac)_2$ were added to a round-bottom flask, and dried in the oven at 100 ℃ for 30 min. Then, 126.0 mL glycerol was added to obtain the $Ni(Ac)_2$/glycerol solution (10 g/L). The solution was magnetically stirred for 15 minutes at room temperature and then sonicated for 30 min. Then, the solution was magnetically stirred once again overnight to obtain a homogeneous green solution.

The solution was then refluxed for 40 minutes at a temperature around the boiling point of glycerol (290 ℃). The temperature was carefully controlled using a heating mantle (Glass-Col TM106) and heat isolating sand. During the experiment, the mantle and heat isolating sand was first preheated to 270 ℃. After that, the round bottom flask was

immersed into the sand. More sand was added then in such a way that the flask was fully embedded in the sand. Then, the temperature was slowly raised up to 290 °C. Figure 3.2 shows the experimental observations during the NMF synthesis reaction.

When the temperature reached to 290 °C, small bubbles were generated from the bottom. During the first 4 minutes, Ni^{2+} particles started to aggregate and forms small sponge-like materials. In the next 6 min, the solution turned black indicating that most of the Ni^{2+} ions were reduced to metallic Ni^{0}.

Fig 3.2 Experimental observations during the synthesis of raw NMF

By continuing the reflux, the Ni particles began to aggregate forming two distinct phases of a spongy structured Ni and a dark golden solution was then kept refluxing for 20 additional minutes to ensure the reaction was complete. To maintain a consistent reproduction of the synthesis, precise temperature control is imperative. Otherwise, the

over-reflux would lead to the destruction of the micro-structures due to the over boiling. The temperature was always kept at 290 ℃ ± 10 ℃. At the end of the reaction, black sponge-like magnetic pieces of Ni foam floated on the top of the solution. The homogeneity of $Ni(Ac)_2$/glycerol solution is also a critical parameter. Insufficient stirring or mixing of the solution result into unreacted $Ni(Ac)_2$ residue powder, and affect the formation of spongy structured Ni foam.

Once the solution was cooled down to room temperature, the as-synthesized materials were collected and washed with deionized water (18.5mΩ) for several times. The product is referred to as as-prepared Ni foams.

As previously mentioned, the present reaction temperature was set to 290 ℃. This is the boiling point of the reducing agent (glycerol). However, it was hypothesized that increasing the reaction temperature could reduce the time of crystalline procedure and therefore might benefit the formation of a foam structure. Therefore, the experiment was performed at different temperature (290, 320, 350, and 400℃), and the resulting materials were analyzed. It was found that, at increased temperatures above 290 ℃, the time for the reduction of Ni^{2+} and aggregation stage (from t = 0min to t ≈ 10min at 290 ℃) was reduced to less than 8 mins. At the crystalline stage of the reaction, due to the oxidation of the glycerol, the viscosity and boiling of the liquid phase significantly dropped, causing the over boiling of the solution. Due to the fierce bubbling and large drops of cooled solution from the reflux tube, particles were hardly aggregating. Taking all these factors into consideration, 290 ℃ can be considered as an optimized temperature for synthesizing as-

synthesized NMF.

In addition to the reaction temperature, the concentration of the $Ni(Ac)_2$/glycerol solution used in the raw Ni foam synthesis was also optimized, e.g. 20, 40, 60, and 100 mM. The CV results of these raw Ni foam obtained at different concentration were displayed in supporting materials. Overall, the Ni foams obtained using the 40 mM $Ni(Ac)_2$/glycerol solution showed the best performance.

The $Ni(Ac)_2$ precursor in the amount of 0.9996g was added to the round bottom flask to prepare the 40 mM/L nickel acetate/glycerol solution. The yield of NMF could be calculated based on the Eq.3.1:

$$\boldsymbol{Yield = \frac{mass\ of\ Ni^0 product}{mass\ of\ Ni^{2+} in\ precurcor}} \qquad \boldsymbol{Eq(3.1)}$$

The mass of Ni^0 from obtained NMF products was 0.207 g while the initial mass of the Ni^{2+} in the precursor was 0.236 g. The eventual yield is calculated to be 88 ~ 90%.

3.2.2Heat treatment of as-prepared NMF

The heat treatment was applied to produce NiO wires, Nickel meso-foams after direct H_2 treatment (NMF-H_2) and Nickel meso-foam after O_2/H_2 treatment (NMF-O_2/H_2) from as-synthesized NMF. The treatment was performed in a quartz reactor under an airflow (20% oxygen, 80% nitrogen, Linde, 99.999%) of 25 $mL \cdot min^{-1}$.

In the oxidation process, the quartz reactor was slowly heated at a rate of 10 ℃$\cdot min^{-1}$. Once the temperature reached 600 ℃, it was held constant for 4 h. After the reactor slowly cooled down back to room temperature, the oxidized product NiO was collected for

further treatment. The purpose of carrying out this oxidation treatment was to obtain a relatively pure oxidized Ni phase.

In the reduction experiment, both as-prepared NMF and NiO were reduced with pure H_2 (Linde, 99.999%). First, the reactor was purged with N_2 (Linde, 99.999%) at room temperature for 30 minutes at a flow rate of 30 $mL \cdot min^{-1}$ to remove air, then H_2 flow was introduced at a rate of 20 $mL \cdot min^{-1}$. At the same time, the reactor was heated to 300 °C with a ramping rate of 10 $°C \cdot min^{-1}$. The temperature was maintained at 300 °C for 2 h. After that, inlet gas was switched from H_2 to N_2 and the reactor was cooled down to room temperature in case of the re-oxidation once H_2 was cut down. The products were collected then crashed into powders and kept in the vial for further use.

3.2.3Physicochemical characterizations

Scanning Electron Microscopy (SEM)

The SEM characterizations were carried out on a JSM-7500F FESEM instrument with an acceleration voltage of 2 kV and 3 kV. The surface morphology of the materials was studied at the magnifications that ranged from 800 to 30,000.

X-ray Diffraction (XRD)

The XRD patterns of as-prepared NMF, NiO and NiMF-O_2/H_2 samples were collected on a RigakuUltima IV diffractometer using a CuKa X-ray source (40 kV, 40 mA). The measurements were carried out at a scan rate of 0.033 degree (2θ)/s between 20 to 80 º2θ.

XRD is a measurement that aimed to investigate the crystal structure of the Ni sponge

materials. It can be also used to calculate the average diameter of the nanoparticles. The position of the XRD peaks is related the inter-planar distance of the different crystalline planes, the size of nanoparticles can be calculated using the Scherrer equation, Eq 3.2:

$$\boldsymbol{D = K\lambda/\beta cos\theta} \qquad \boldsymbol{Eq(3.2)}$$

In this equation, ***D (nm)*** is the mean size of the crystallite particles; ***K*** is the dimensionless shape factor which generally is integer as 0.94; ***λ(nm)*** is the wavelength of the X-ray source applied which in our characterizations was CuKα with a wavelength of 1.54 Å; ***β(rad)*** is the line broadening at half the maximum intensity (FWHM) after subtracting the instrumental line broadening. β is expressed in radians; ***θ*** is the Bragg angle in degrees.

Transmission Electron Microscopy (TEM)

The TEM images of Ni-based materials were obtained using a JEM-2100F FETEM instrument at an acceleration voltage of 120 kV. The TEM samples were prepared by using ultrasound sonication to thoroughly disperse the catalyst powder into ethanol/water solution. Then, the top suspension was dropped onto the copper grid and air-dried for TEM analysis.

3.2.4 Electrochemical Characterizations

The electrochemical performance of the Ni-based materials was evaluated by using a potentiostat/galvanostat (Bio-Logic VSP Ultimate Electrochemical Workstation) with the EC-Lab software package. A three-electrode Teflon cell was used for all electrochemical

experiments. The cell consisted of a glassy carbon (GC) working electrode (geometric area of 0.196 cm^2), a mercury/mercury oxide (Hg/HgO) reference electrode, and a Pt mesh counter electrode. All the electrochemical tests were carried out in the reference of a mercury/mercury oxide (Hg/HgO) electrode.

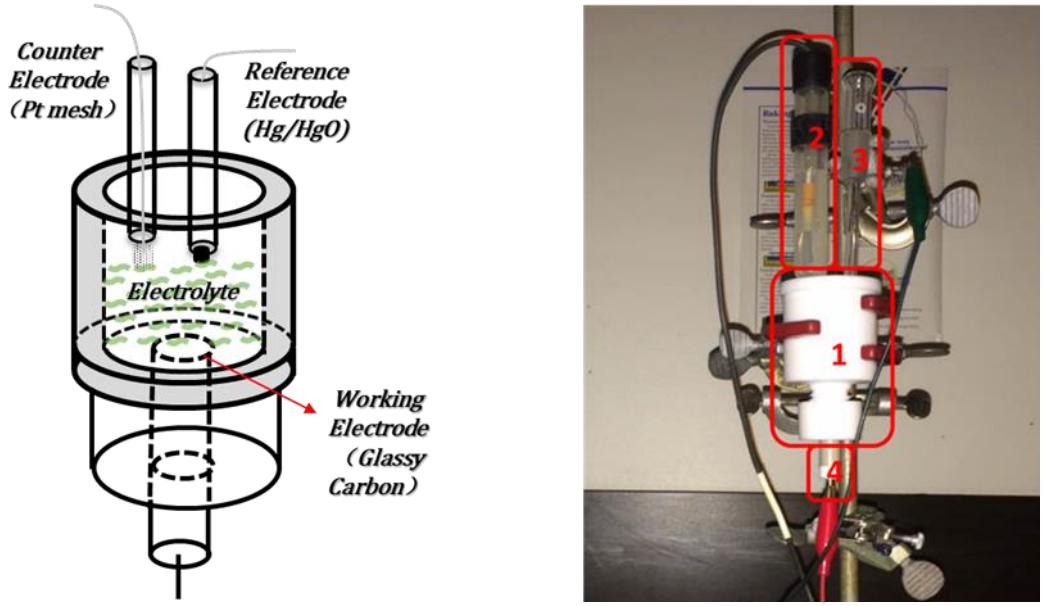

Figure 3.3 Experimental Setup. Left: Schematic cell setup; Right: Experimental cell: 1) tri-electrodes Teflon Cell System, 2) Mercury/Mercury Oxide (Hg/HgO) reference electrode, 3) Pt mesh counter electrode, 4) Glassy carbon working electrode.

The preparation of the working electrode involved a coating procedure to deposit the catalysts on the GC electrode. A catalyst ink-solution was made by mixing 6 mg of the crushed Ni sponge, 1.0 mL of deionized water (18.5mΩ·cm^{-1}), 200 µL of isopropanol (Fisher Scientific, 99.5%), and 100 µL of Nafion solution (Sigma Aldrich, 5wt%). The ink was then sonicated for 30 minutes to ensure it was homogenous. Ten µL of the ink were dropped on the surface of the GC working electrode using a pipette. The coated electrode was air-dried in an oven at 60°C for five minutes.

Electrochemical Measurements

Chronoamperometry (CA), cyclic voltammetry (CV), and linear sweep voltammetry (LSV) measurements were all performed in 1 M KOH solution. Electrochemical results are referred to the mercury/mercury oxide (Hg/HgO) reference electrode to study the catalytic performance of NMF materials toward OER. For accuracy, all data used for calculations were collected from the 10th cycle of each electrochemical procedure. First, a CA polarization procedure was performed to remove the surface oxides/hydroxides by adding a potential of -1.3 V for five minutes. Then, a CA procedure under E = -0.8 V for 10 minutes was applied to reduce the trace of generated H_2 (gas) during the polarization time, as suggested by the work of M. Houache et al. and G. Jerkiewicz et al. [15,16]. The last CA procedure was applied to study the behavior and stability of catalysts in the OER region under a constant potential of 0.7 V for 1 hour vs the Hg/HgO reference electrode.

Cyclic voltammetry results were acquired by applying different potential windows. The cathodic region CVs were obtained by scanning from -0.95 V to -0.4 V at a scan rate of 50 mV·s^{-1}. The data collected from CVs was then normalized and calculated to determine the electrochemical active surface area (ECSA) of as-prepared NMF, NMF-H_2, and NMF-O_2/H_2, the method of which was proposed by S. A. S. Machado et al. [17]. In calculating the ECSA, the total charge $Q_c(mC)$ was calculated by the following equation:

$$\boldsymbol{Q = \int I(E) dE \cdot 10^3 / [dE/dt\ (Scan\ rate)]} \qquad \boldsymbol{Eq(3.3)}$$

The integral of $I(A)$ vs $E(V)$ (i.e. the area under the curve) was defined over the

selected potential window via Simpson's integration method. Usually, the potential window for Ni materials can be set from -0.75 V to -0.55 V. Then, the ECSA (cm^2) can be calculated by dividing Q by the theoretical constant of 0.514 $mC \cdot cm^{-2}$:

$$\boldsymbol{ECSA = Q\ /0.514} \qquad \boldsymbol{Eq(3.4)}$$

Followed by the tests in the cathodic region, CVs in a potential window from -0.95 V to 0.65 V was then performed to obtain a whole potential window scale performance from the cathodic region to the anodic region at a series of scan rates of 300, 200, 150, 100, 50, and 20 $mV \cdot s^{-1}$. The CVs of the anodic region were obtained at a potential window from 0.1 V to 0.65 V. The electrochemical performance in the anodic region was used for illustrating and discussing the transformation of different Ni oxide phases. Finally, to test the OER performance, CVs in a potential window from 0.1 V to 1.2 V were applied. [20]

The linear sweep voltammetry measurements were carried out at a scan rate of 1 $mV \cdot s^{-1}$ with a potential window from 0.3 V to 1.0 V. The LSV data was normalized and used to picture the Tafel plots, in which the Tafel slope and overpotential are the two essential parameters in evaluating the OER activity of the catalysts. To compare the activities toward OER, all currents in CA, CV, LSV, and Tafel plot measurements were normalized by the geometric area (0.196 cm^2).

3.3 Results and Discussion

3.3.1 Physicochemical Properties of Ni-based Meso-foams

SEM Characterization

Information about the surface morphology and size of these materials was provided by SEM characterizations. Synthesized NMF shows a rather high porosity. The smaller building blocks of NMF offer greater porosity and a larger surface area, which is capable of enhancing the loading of other catalysts and promoting the catalytic capability towards OER.

Figure 3.4 (b, c) shows that the size of the NMF-H_2 particle was maintained at a size similar to that of the raw NMF. Some cracks and scratches can be observed in Figure 3.4 (b), corresponding to the volume variation of NMF after the H_2 reduction procedure. Physical characterizations of the NMF-O_2/H_2 were performed, as seen in Figure 3.4 (d, e), which shows morphology changes after the reduction process and oxidation/reduction process. The average wire diameter of the NMF- O_2/H_2 significantly increased to 500 nm – 2 μm, compared to raw NMF and NMF-H_2. Meanwhile, a large number of nano-sized pores and cracks were generated on the surface of the wires. The reason for the formation of the cracked, semi-hollow surface morphology from NMF-O_2/H_2 might be related to the Kirkendall effect during the oxidation process, which would have resulted from the fast outward diffusion of Ni through the initial oxide layer on the surface [11,12]. TEM information of NMF-O_2/H_2 was obtained from Figure 3.4 (f) and further confirmed that the NMF-O_2/H_2 wire was composed of aggregated fine nanoparticles with a diameter of ~30 nm. The dark black inside surrounded by a shallow core-shelled structure is very clearly exhibited at the top side of the graph, which indicates that the synthesis of this 3D porous material was a success.

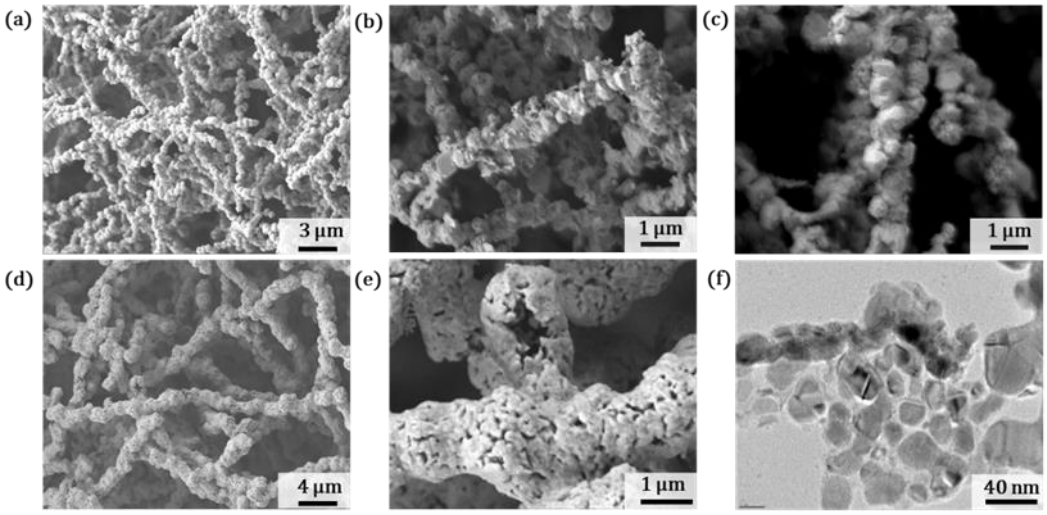

Figure 3.4 SEM results of surface morphologies of the (a) raw NMF, (b, c) NMF-H_2 and (d, e) NMF-O_2/H_2, and (f) TEM images of NMF-O_2/H_2.

XRD Characterization

Figure 3.5 shows the XRD pattern of raw NMF, NiO, and NMF-O_2/H_2 samples, in which the three peaks at 44.4°, 53.8°, and 77.6° are corresponding to the (111), (200), and (220) planes of face-centered cubic phase Ni (JCPDS card no. 04-0850). The NiO wires exhibit distinctive peaks at 37.3°, 43.1°, 63.6°, 75.8°, and 79.4°, corresponding to the (111), (200), (220), (311), and (222) planes of fcc-structured NiO, respectively (JCPDS card no. 47-1049), indicating the successful formation of NiO after the oxidation of raw NMF. The calculated crystallite sizes of NMF, NiO, and NMF-O_2/H_2 were 71.28 nm, 119.58 nm, and 90.43 nm, respectively.

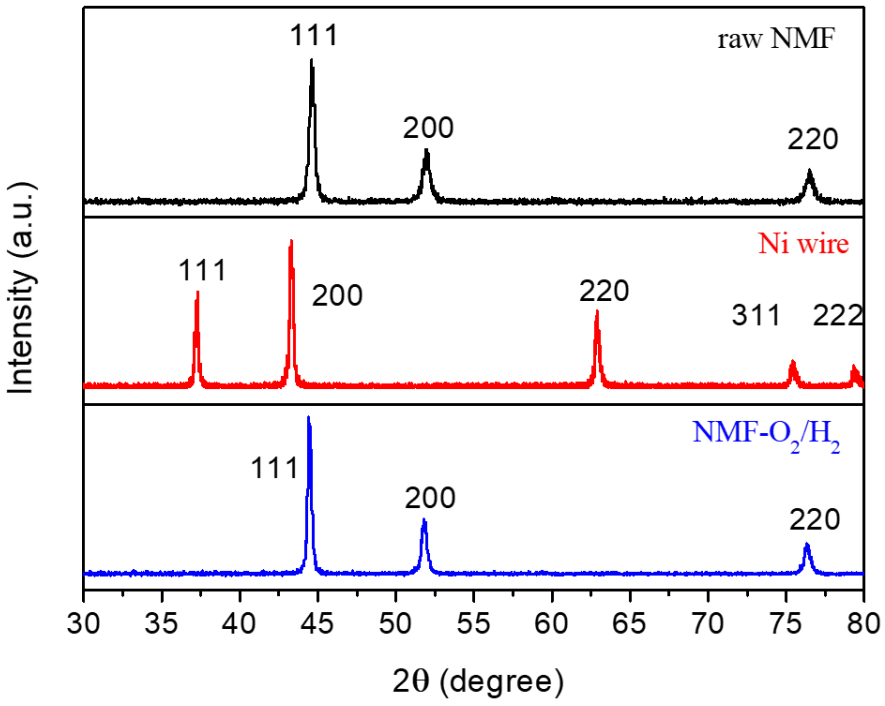

Figure 3.5 XRD measurement results of (a) raw NMF, (b) Ni wire, and (c) NMF-O_2/H_2.

3.3.2 Electrochemical Performance

ECSA and CV in the Cathodic Region

In Figure 3.6, the CV curve of NMF-O_2/H_2 exhibits a larger potential hysteresis with two redox peaks broader than that of NMF and NMF-H_2. Meanwhile, NMF-O_2/H_2 also shows the largest peak area in the CV profile, suggesting its increased ECSA in the three materials. Table 3.1 shows the calculated ECSA of the raw NMF, NMF-H_2, and NMF-O_2/H_2 materials.

Table 3.1 The ECSA results of the raw NMF, NMF-H_2, and NMF-O_2/H_2 in the cathodic region in 1 M KOH, 50 mV·s^{-1}.

Material	ECSA (cm^2)	ECSA (cm^2/g)
Raw NMF	0.0031	0.0664
NMF-H_2	0.0508	1.1004
NMF-O_2/H_2	0.5303	11.4916

The ECSA of NMF, NMF-H_2, and NMF-O_2/H_2 are 0.0031 cm^2, 0.0508 cm^2, and 0.5303 cm^2, respectively. The significantly increased ECSA of NMF-O_2/H_2 suggests that the oxidation procedure is effective in creating semi-hollows and, therefore, enlarges the active surface area of the materials.

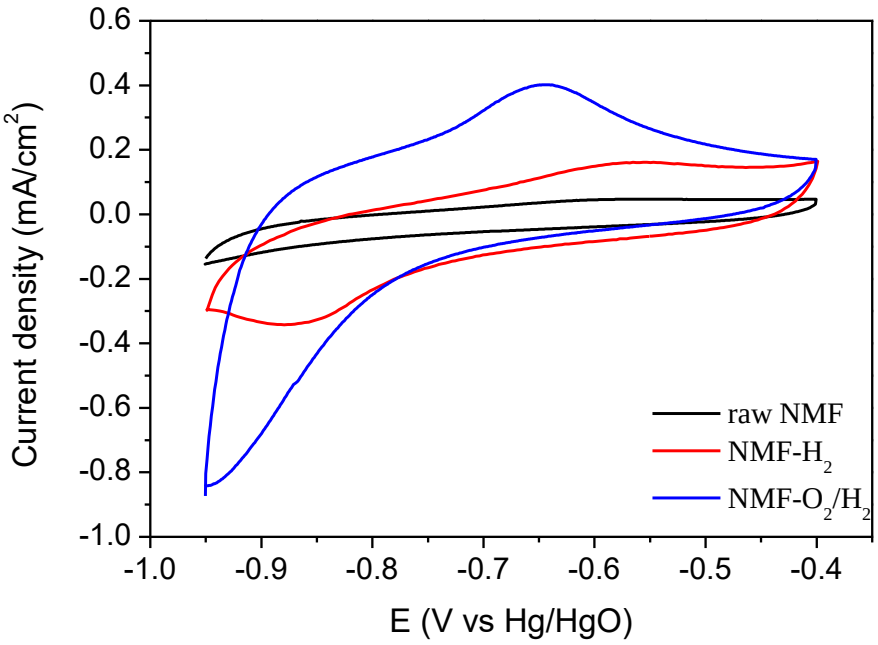

Figure 3.6 CV results of the raw NMF, NMF-H_2, and NMF-O_2/H_2 in the cathodic region in 1 M KOH. Scan rate = 50 mV·s^{-1}.

Additionally, reproducibility tests on the ECSA of NMF-O_2/H_2 were carried out (see Figure 3.7 and Table 3.2). The reproducibility tests were intended to confirm the reliability of the experimental procedures and the performance of the materials. The detailed ECSA results of the three trails tests can be found in Table 3.2.

Table 3.2 Reproducibility tests on the ECSA results of NMF-O_2/H_2

Trials	ECSA (cm^2)	ECSA (cm^2/g)
1	0.5243	11.2763
2	0.4137	8.9642
3	0.5042	10.9254
Avg.	0.4807	10.3886

The ECSA of NMF-O_2/H_2, calculated from three different trials, are 0.5303 cm^2, 0.4137 cm^2, and 0.5042 cm^2, respectively. The average value of ECSA is 0.4807 cm^2 (10.9254 cm^2/g). The difference between the highest and average value is 9.07 %, and the deviation from the lowest value is 13.93 %. Thus, the deviation of the reproducibility trials was in an acceptable range, suggesting that the experiments are reliable.

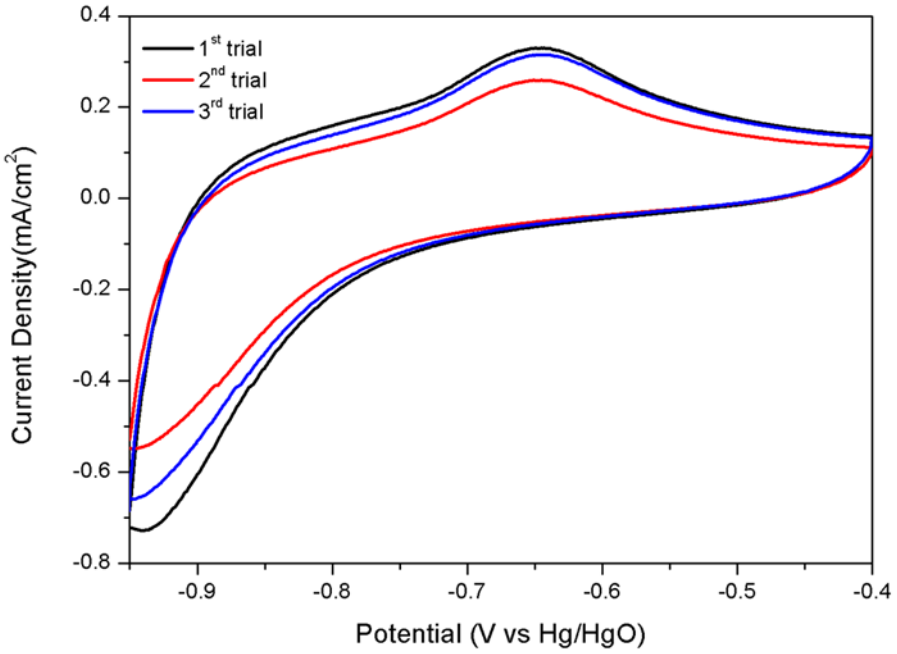

Figure 3.7 CV results of the reliability tests on the NMF-O_2/H_2 in the anodic region. Scan rate = 50 $mV \cdot s^{-1}$; electrolyte = 1 M KOH.

Electrochemical Performance of Oxygen Evolution Reaction

The Bode diagram (Figure 3.8) presents the complete schematic of Ni oxides transformations in catalyzing OER in an alkaline solution [19]. First, the unstable α-$Ni(OH)_2$ state is oxidized into stable β-$Ni(OH)_2$ after prolonged exposure in an alkaline condition. Further polarization induces the deprotonation of β-$Ni(OH)_2$ and forms β-NiOOH, which is usually considered the active phase for OER [18]. Further increasing the electrode

potential will overcharge the β-NiOOH and convert it into the highest oxidation state, γ-NiOOH.

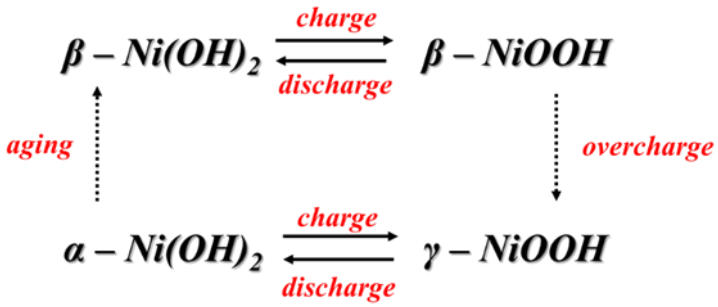

Figure 3.8 Schematic of the transformation of Ni oxides during OER in alkaline condition [19].

Figure 3.9 shows that the initiation potentials of peak transformation (from β-$Ni(OH)_2$ to β-NiOOH) of raw NMF and NMF-O_2/H_2 were basically the same (around 0.42 V). However, as compared to that of the raw NMF and NMF-H_2, NMF-O_2/H_2 materials exhibit a huge and uniformed transformation peak, from β-$Ni(OH)_2$ to β-NiOOH, which might result from the oxidation of non-reduced compositions. In addition, compared to the raw NMF and NMF-H_2, the peak of NMF-O_2/H_2 was sharp; a possible reason is that some of the oxides, which take part in the transformation procedure, were reduced to metallic Ni and then formed into α-phase during the CV scan. Figure 3.1 also shows that the initiation potential of NMF-H_2 was shifted to the higher potential point, which is around 0.47 V, compared to the NMF-O_2/H_2, and that the peak potential shifted from 0.44 V to 0.52 V, respectively. In conclusion, the Ni oxides and other Ni compounds on the raw NMF formed in the synthesizing procedure affected the transformation peak of the β-$Ni(OH)_2$ to β-NiOOH phase. Ni oxides would only affect the size of the peak. At the same time, the CV

curves of raw NMF and NMF-H_2 confirmed that the unknown Ni compounds affected the peak potential of the transformation from β-$Ni(OH)_2$ to β-NiOOH, as revealed by the peak shift in the NMF-O_2/H_2 sample.

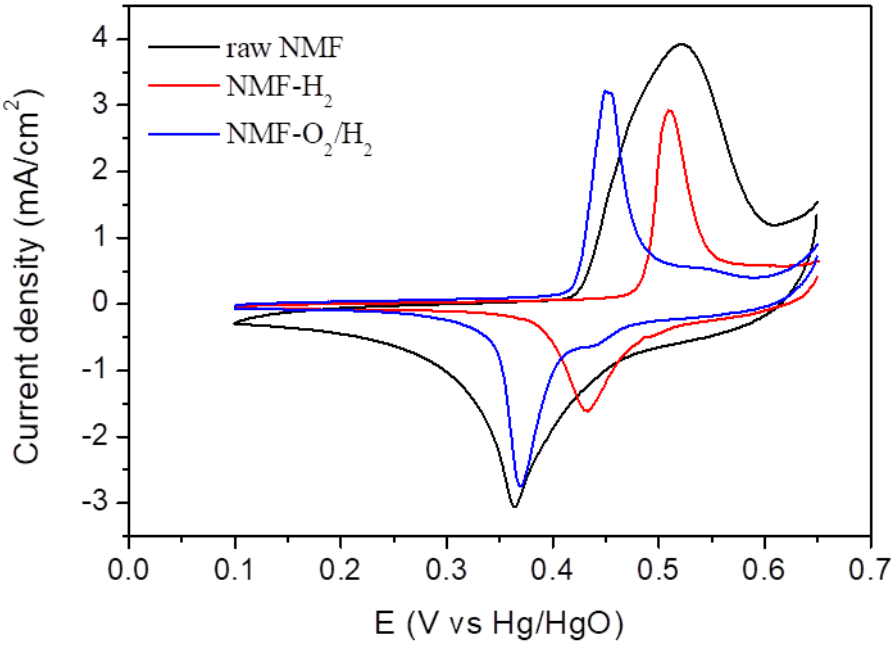

Figure 3.9 CV results of the raw NMF, NMF-H_2, and NMF-O_2/H_2 in the anodic region. Scan rate = 50 mV·s^{-1}; electrolyte = 1 M KOH.

Figure 3.10 shows the CV of the three catalysts in the OER region. The current density obtained at 1.2 V for raw NMF, NMF-H_2, and NMF-O_2/H_2 was 77.64 mA/cm^2, 86.45 mA/cm^2, and 108.66 mA/cm^2, respectively. That is, NMF-O_2/H_2 exhibits the highest current density among these catalysts, suggesting its high OER activity.

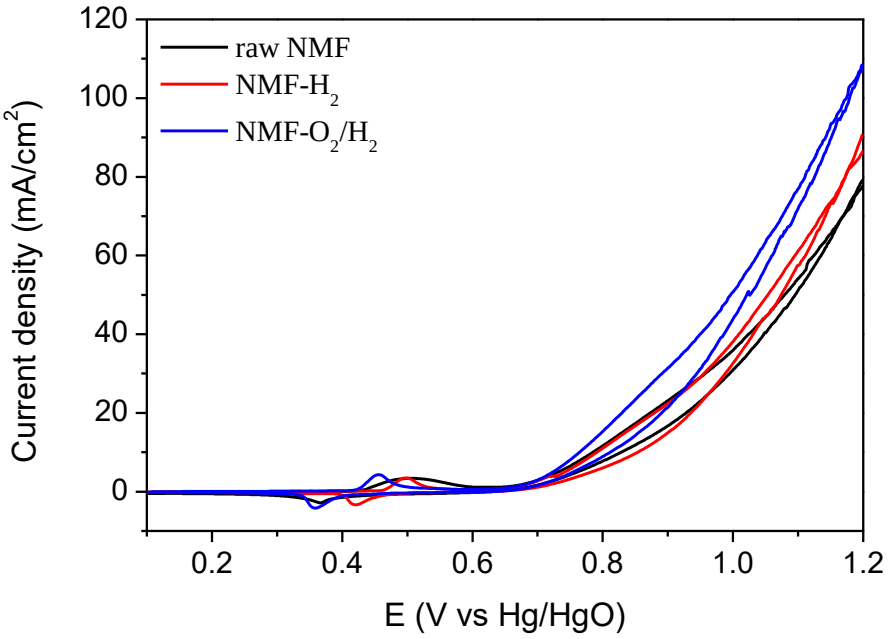

Figure 3.10 CV of the raw NMF, NMF-H_2, and NMF-O_2/H_2 in the OER region. Scan rate = 50 mV·s^{-1}; electrolyte = 1 M KOH.

LSV and Tafel Plots

As shown in Figure 3.13, the LSV curves indicate that NMF-O_2/H_2 exhibits the highest activity among the as-prepared catalysts. For example, when a current density of 10 mA/cm^2 is generated, it has the lowest overpotential of ~364 mV, slightly less than the overpotential of NMF-H_2, which is ~388 mV, and less than the over potential of raw NMF, which is ~389 mV. This can be attributed to the enlarged surface area. The Tafel plot (Figure 3.14) also further confirmed the best OER activity of NMF-O_2/H_2, with a much smaller slope of 62.91 mV.dec^{-1}. After the calculation, the exchange current density of the three materials reviewed in this chapter was 5.65×10^{-4}A cm^{-2}, 5.63×10^{-5}A cm^{-2}, and 7.69×10^{-5}A cm^{-2}.

Electrochemical results are collected and exhibited in table 3.3. It is obviously to say that the NMF-O_2/H_2 shows the best performance among all the NMF materials which is recommended to have further modifications and studies.

Table 3.3 Collection of electrochemical results

Catalysts	Tafel slope ($mV.dec^{-1}$)	Overpotential (mV)	Exchange current density ($A\ cm^{-2}$)
Raw NMF	69.45	389	5.65×10^{-4}
NMF-H_2	67.13	388	5.63×10^{-5}
NMF-O_2/H_2	62.91	364	7.69×10^{-5}

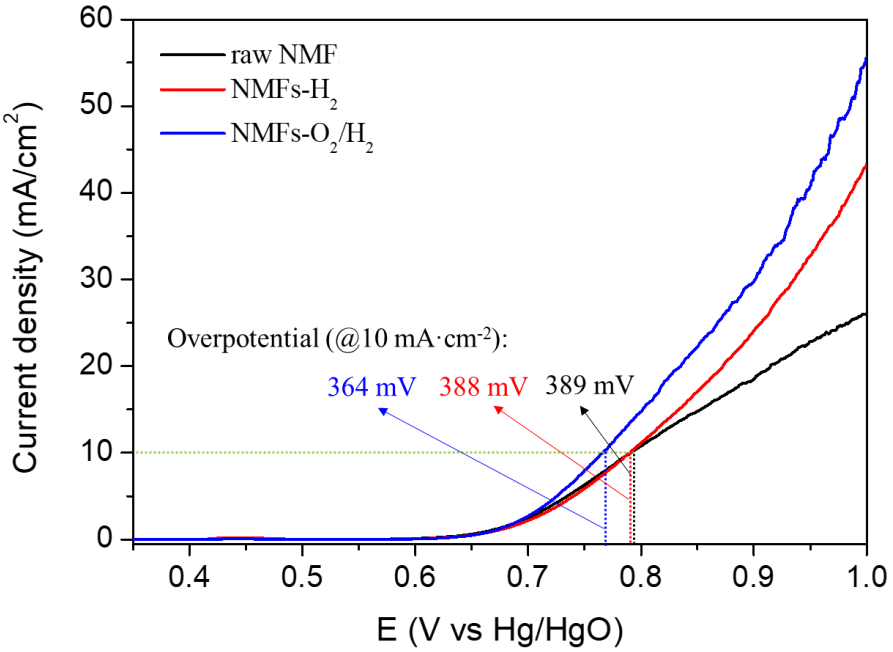

Figure 3.13 LSV results of the raw NMF, NMF-H_2, and NMF-O_2/H_2 in the OER region. Scan rate = 1 $mV{\cdot}s^{-1}$; electrolyte = 1 M KOH.

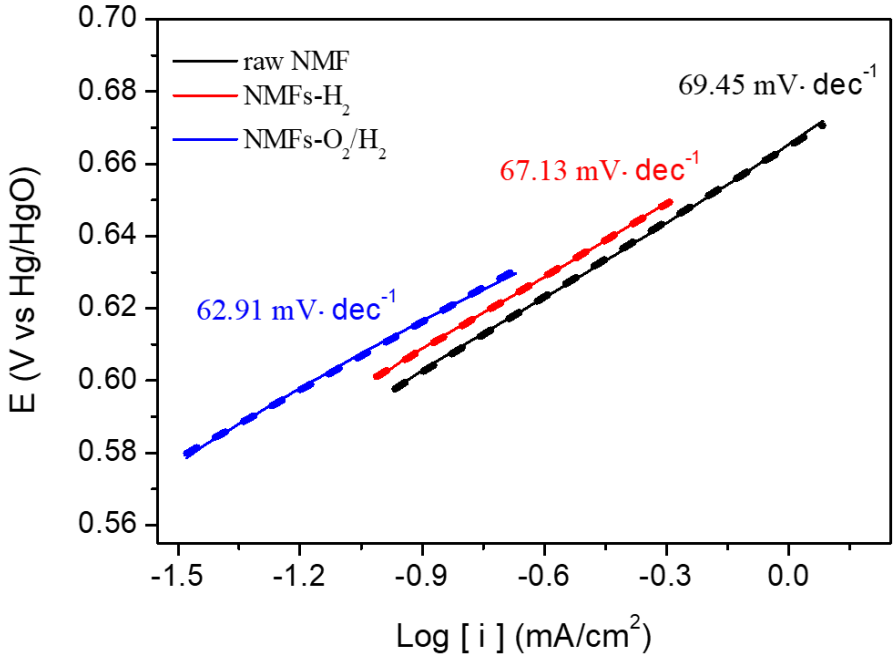

Figure 3.14 Tafel plots of the raw NMF, NMF-H_2, and NMF-O_2/H_2. Scan rate = 1 mV·s^{-1}; electrolyte = 1 M KOH.

3.4 Summary

In this chapter, a porous crosslinking Ni meso-foam was successfully synthesized via a simple chemical reduction procedure using glycerol as a reducing and stabilizing agent. To have more porous structures and electrochemically active reacting sites, a heat treatment procedure was introduced for producing reduced NMF, which is referred to as NMF-H_2 and NMF-O_2/H_2. From SEM characterizations, the as-synthesized and heat-treated materials showed porous morphology and a cross-linking wired structure; additionally, the XRD results confirmed the composition of Ni^0 after the complete oxidation and reduction

process.

The electrochemical catalytic capability of the synthesized NMF was evaluated. First, after heat treatment, the ECSA of these NMF materials exhibit a significant promotion compared to the untreated raw NMF, suggesting the formation of the more catalytic sites. Moreover, it was found that the NMF-O_2/H_2 catalyst exhibits the lowest Tafel slope (62.91 $mV.dec^{-1}$) and overpotential (364 mV) among the as-prepared materials. All the physiochemical and electrochemical measurements indicate that the synthesized NMF materials were in considerable catalytic capability. The following chapters will show how they were modified to further increase their OER activity.

Reference

[1]. Zheng, Y., Jiao, Y., Vasileff, A., & Qiao, S. Z. (2018). The Hydrogen Evolution Reaction in Alkaline Solution: From Theory, Single Crystal Models, to Practical Electrocatalysts. Angewandte Chemie - International Edition, 57(26), 7568–7579.

[2]. Shi, Y., & Zhang, B. (2016). Recent advances in transition metal phosphide nanomaterials: Synthesis and applications in hydrogen evolution reaction. Chemical Society Reviews, 45(6), 1529–1541.

[3]. Liu, G., Li, J., Fu, J., Jiang, G., Lui, G., Luo, D., Deng, Y.-P., Zhang, J., Cano, Z. P.,

Yu, A., Su, D., Bai, Z., Yang, L., & Chen, Z. (2019). Zinc-Air Batteries: An Oxygen-Vacancy-Rich Semiconductor-Supported Bifunctional Catalyst for Efficient and Stable Zinc-Air Batteries (Adv. Mater. 6/2019). Advanced Materials, 31(6), 1970043.

[4]. Li, J. C., Hou, P. X., Zhao, S. Y., Liu, C., Tang, D. M., Cheng, M., Zhang, F., & Cheng, H. M. (2016). A 3D bi-functional porous N-doped carbon microtube sponge electrocatalyst for oxygen reduction and oxygen evolution reactions. Energy and Environmental Science, 9(10), 3079–3084.

[5]. Lui, G., Li, G., Wang, X., Jiang, G., Lin, E., Fowler, M., Yu, A., & Chen, Z. (2016). Flexible, three-dimensional ordered macroporous TiO2 electrode with enhanced electrode–electrolyte interaction in high-power Li-ion batteries. Nano Energy, 24, 72–77.

[6]. Hao, M., Charbonneau, V., Fomena, N. N., Gaudet, J., Bruce, D. R., Garbarino, S., Harrington, D. A., & Guay, D. (2019). Hydrogen Bubble Templating of Fractal Ni Catalysts for Water Oxidation in Alkaline Media [Research-article]. ACS Applied Energy Materials, 2(8), 5734–5743.

[7]. Zhu, L. P., Liao, G. H., Yang, Y., Xiao, H. M., Wang, J. F., & Fu, S. Y. (2009). Self-assembled 3D flower-like hierarchical β-Ni(OH) 2 hollow architectures and their in situ thermal conversion to NiO. Nanoscale Research Letters, 4(6), 550–557.

[8]. Zhu, T., Koo, E. R., & Ho, G. W. (2015). Shaped-controlled synthesis of porous NiCo2O4 with 1-3 dimensional hierarchical nanostructures for high-performance supercapacitors. RSC Advances, 5(3), 1697–1704.

[9]. Qiao, Y., Jia, P., Zhang, X., Xi, J., Hao, X., Tang, Y., & Wang, X. (2015). Template-free synthesis of mesoporous nickel oxide electrode material with three-dimensional flowerlike morphology. Electrochimica Acta, 186, 314–320.

[10]. Chen, S., Duan, J., Bian, P., Tang, Y., Zheng, R., & Qiao, S. Z. (2015). Three-Dimensional Smart Catalyst Electrode for Oxygen Evolution Reaction. Advanced Energy Materials, 5(18), 1–7.

[11]. Ni, W., Wu, H. Bin, Wang, B., Xu, R., & Lou, X. W. (2012). One-pot synthesis of ultra-light nickel nanofoams composed of nanowires and their transformation into various functional nanofoams. Small, 8(22), 3432–3437.

[12]. Ni, W., Wang, B., Cheng, J., Li, X., Guan, Q., Gu, G., & Huang, L. (2014). Hierarchical foam of exposed ultrathin nickel nanosheets supported on chainlike Ni-nanowires and the derivative chalcogenide for enhanced pseudocapacitance. Nanoscale, 6(5), 2618–2623.

[13]. Xia, X. H., Tu, J. P., Zhang, J., Wang, X. L., Zhang, W. K., & Huang, H. (2008). Electrochromic properties of porous NiO thin films prepared by a chemical bath deposition. Solar Energy Materials and Solar Cells, 92(6), 628–633.

[14]. Wu, M. S., & Yang, C. H. (2007). Electrochromic properties of intercrossing nickel oxide nanoflakes synthesized by electrochemically anodic deposition. Applied Physics Letters, 91(3).

[15]. Houache, M. S. E., Cossar, E., Ntais, S., & Baranova, E. A. (2018). Electrochemical modification of nickel surfaces for efficient glycerol electrooxidation. Journal of

Power Sources, 375(December), 310–319.

[16]. Grdeń, M., Alsabet, M., & Jerkiewicz, G. (2012). Surface science and electrochemical analysis of nickel foams. ACS Applied Materials and Interfaces, 4(6), 3012–3021.

[17]. Machado, S. A. S., & Avaca, L. A. (1994). The hydrogen evolution reaction on nickel surfaces stabilized by H-absorption. Electrochimica Acta, 39(10), 1385–1391.

[18]. Fabbri, E., Habereder, A., Waltar, K., Kötz, R., & Schmidt, T. J. (2014). Developments and perspectives of oxide-based catalysts for the oxygen evolution reaction. Catalysis Science and Technology, 4(11), 3800–3821.

[19]. Bode, H.; Dehmelt, K.; White, J. Zur kenntnis der nickelhydroxidelektrode—I.Über das nickel (II)-hydroxidhydrat. Electrochim. Acta 1966, 11, 1079–1087.

[20]. Cossar, E., Houache, M. S. E., Zhang, Z., & Baranova, E. A. (2020). Comparison of electrochemical active surface area methods for various nickel nanostructures. Journal of Electroanalytical Chemistry, 870, 114246.

Chapter 4 - $Ni/Ni(OH)_2$-Layered Structure Materials for OER

This chapter details how a dynamic hydrogen bubble templating (DHBT) electrodeposition and etching method was applied to fabricate porous $Ni/Ni(OH)_2$ catalysts. The effect of electrodeposition potentials on the surface morphology of $Ni/Ni(OH)_2$ and their corresponding electrochemical performance was investigated. Specifically, SEM characterizations were utilized to better understand the surface and interface topographical and morphological information of this material. In addition, electrochemical tests, such as CV and LSV, were adapted to examine electrochemical performance, including current density, OER onset potential, and overpotential of the porous Ni_{DHBT} materials. Among all investigated materials, the Ni_{DHBT} (-4 V) catalyst shows the best OER activity: it has an overpotential of 277 mV at 10 $mA{\cdot}cm^{-2}$ in 1M KOH.

4.1 Introduction

Electrochemical water splitting is a promising method for producing H_2 gas, which is a clean and renewable energy source. However, in a water electrolyzer, the slow OER kinetics limit the overall efficiency of the water splitting process [1]. Recently, nickel hydroxides have attracted much attentions due to their good OER catalytic activity and stability in alkaline media, and various nickel hydroxides catalysts with different particle sizes and morphologies have been developed [2]. Previous studies have also demonstrated that, in addition to its intrinsic catalytic properties, the micro-porous design of the catalysts

plays an important role in improving its OER activity. The micro-porous structure not only provides an increased surface area for the active sites, but also it facilitates the mass transportation at the gas/solid/electrolyte three-phase interface, at which the OER occurs [3-5].

The most widely reported methods for synthesizing nickel hydroxides are hydrothermal reaction and anodic deposition. The latter has the advantage of the weight and thickness of the nickel hydroxides film that may be easily controlled by tuning the current and composition of the electrolyte [6]. Meanwhile, DHBT is an efficient method to develop 3D porous metals [7]. Thus, it would be quite interesting to combine electrochemical deposition and hydrogen bubble templating to design a 3D porous Ni hydroxides electrode for the OER.

Therefore, in the present study, a DHBT-assisted electrodeposition method was used to prepare porous Ni/$Ni(OH)_2$-layered substrate, referred to as P-Ni. Then, further deposition of Zn onto P-Ni was performed. The product obtained at this stage is referred to as Zn@P-Ni. Finally, the deposited Zn was etched to obtain a porous Ni_{DHBT} catalyst with enhanced properties toward the OER. In addition, upon varying the electrodeposition conditions, Ni_{DHBT} at different electrodeposition potentials but with similar macroporous structure and morphology was formed. The optimized catalyst is Ni_{DHBT} (-4 V), which is able to deliver a stable overpotential of 277 mV for OER at 10 $mA \cdot cm^{-2}$ in 1M KOH. All the electrochemical results were referred to the Hg/HgO reference electrode.

4.2 Experimental Procedure

4.2.1 Synthesis of Ni/Ni(OH)$_2$-Layered Structure Materials

The synthesis of Ni/Ni(OH)$_2$-layered structures was carried out by a four-step dynamic hydrogen bubble assisted electrodeposition method (the synthesized Ni materials are referred to as Ni$_{DHBT}$). A three-electrode Teflon cell system was used in this experiment (see Figure 4.1). In all deposition steps, a Pt mesh and polished Ni foil with a dimension of 1.44 cm^2 were used as the counter electrode and working electrode, respectively. The working electrode was connected to the power input and EC-Lab potentiostat via a silver wire. The power input was provided by a GW Instek PSH-6018 programmable power supply, which easily allowed us to observe and control the real-time potential and current. Deionized water and analytical-grade chemicals were used in all experimental procedures.

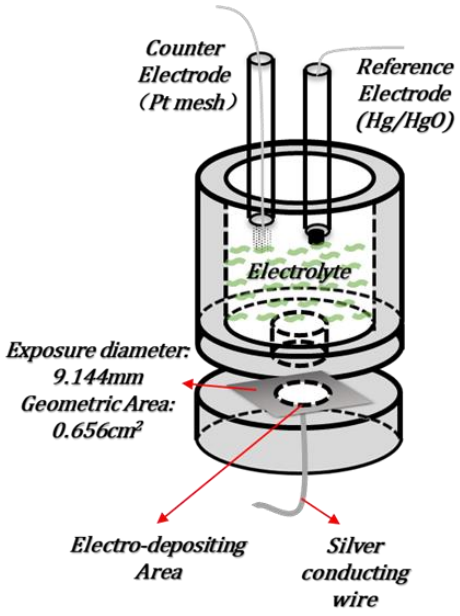

Figure 4.1 Experimental set of working cell.

To better illustrate the synthesis procedure of Ni_{DHBT} materials, a schematic of the preparation procedure is shown in Figure 4.2. Below is a detailed introduction of the synthesis procedure.

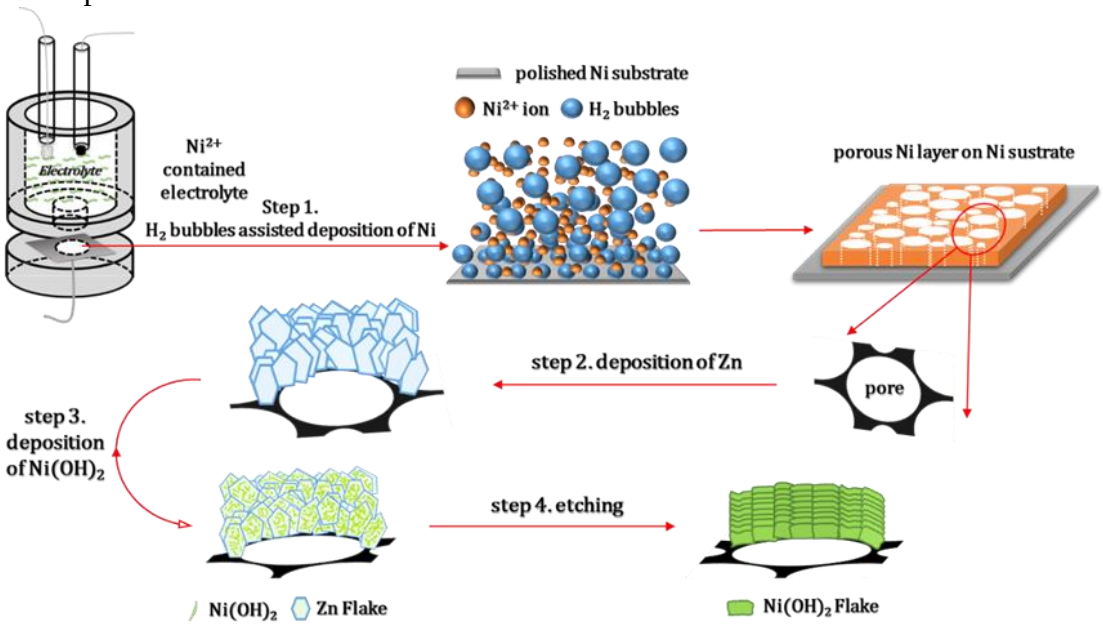

Figre 4.2 Schematic of the synthesis of Ni_{DHBT} catalyst.

Preparation: Polishing Method for Preparing Working Electrode

Ni foil (2.25 cm^2, thickness 0.5 mm, 99.98%, Sigma Aldrich) was initially treated by a physical polishing method by using aluminum oxide in two grades (≥99.0%, 30 μm and 3 μm) to remove its surface roughness and impurities. The polished Ni foil was washed by ultra-sonication in deionized water for five minutes. Then, the Ni foil was soaked in acetone for five minutes to dissolve the organic impurities, followed by four minutes of treatment in nitric acid to remove the inorganic impurities. After that, the Ni foil was rinsed several times with deionized water.

Step 1: Electrodeposition of Porous Structured Ni Layer

Two porous Ni structures were fabricated on the surface of the as-polished Ni foil. This was done through an H_2 bubbles-assisted electrodeposition procedure for 90 seconds under -10 V and -4 V, for both electrodes respectively. The deposition solution was composed of 0.20 M $NiCl_2 \cdot 6H_2O$ (99.99%, Sigma Aldrich), 2.0 M NH_4Cl (99.99%, Sigma Aldrich), and 2.0 M NaCl (99.5%, Sigma Aldrich). After the deposition, the electrodes were rinsed with deionized water several times to prepare for the substrate in the next deposition steps. The two electrodeposited honeycomb-like Ni substrates obtained at different potentials are denoted as P-Ni (-10 V) and P-Ni (-4 V). In this procedure, pores were generated due to the generation of H_2.

Step 2: Electrodeposition of Ni/Zn Platelets

The deposition of Zn platelets onto P-Ni (-10 V) and P-Ni (-4 V) was carried out under a potential -10 V for 12 seconds. The deposition solution contained 0.20 M $ZnCl_2$ (99.999%,

Sigma Aldrich) and 4.8 M KCl (99.0%, Sigma Aldrich). The deposited Zn platelets could be considered as the scaffold to facilitate subsequent growth of $Ni(OH)_2$. The resulting Ni/Zn electrode was rinsed with deionized water several times. Structures acquired after this stage are referred to as Zn@P-Ni (-10 V) and Zn@P-Ni (-4 V).

Step 3: Electrodeposition of Ni/Zn/Ni(OH)$_2$ Composites

The $Ni(OH)_2$ was then deposited on the surface of the as-prepared Zn@P-Ni (-10 V) and Zn@P-Ni (-4 V) platelets at a potential of -1.8 V for 60 seconds. The deposition solution was composed of 0.050 M $NiCl_2$ (99.99%, Sigma Aldrich) and 0.10 M KNO_3 (99.5%, Sigma Aldrich). After the deposition of the $Ni(OH)_2$, the resulting sample was thoroughly rinsed with deionized water. The samples are referred to as $Ni(OH)_2$@Zn@P-Ni (-10 V) and $Ni(OH)_2$@Zn@P-Ni (-4 V).

Step 4: Preparation of Ni/Ni(OH)$_2$ Composites Structure

The last step of the synthesis was to remove the deposited Zn between the porous Ni layer and $Ni(OH)_2$ composites layer. To do this, the as-prepared Ni/Zn/$Ni(OH)_2$ film was immersed in a high-concentration NaOH solution (6 M, 98%, Fisher Scientific) at room temperature for 1 hour. After this etching process, the product was dried at room temperature for 12 hours; the products are referred to as Ni_{DHBT} (-10 V) and Ni_{DHBT} (-4 V).

4.2.2 Physiochemical and Electrochemical Characterizations

The surface morphology, crystal structure and the electrochemical performance toward OER of the catalysts were studied by using SEM, XRD, CA, CV, and LSV

measurements. The detailed setup can be found in Chapter 3.2.3 and 3.2.4.

4.2.3 Electrodeposition Mechanism

Initially, the porous nickel layer was electrochemically deposited via the generation of massive hydrogen bubbles on the surface of the substrate foil. Adsorbed hydrogen atoms were generated by the driving potential (-10V and -4V) during the NH_4^+ discharging process (Equation 4.1). At the same time, with assistance from the generated ammonia, $Ni(NH_3)_x$ complex was formed according to Equation 4.2. Eventually, pores and a metallic nickel layer were created during the discharging of the nickel complex, accompanied by the hydrogen bubbles generation at the substrate surface. See Equation 4.3 and 4.4:

$$NH_4^+ + e^- \rightarrow NH_3 + H_{ad} \qquad Eq(4.1)$$

$$Ni^{2+} + nNH_3 \rightarrow Ni(NH_3)_n^{2+}, 2 \leq n \leq 6 \qquad Eq(4.2)$$

$$2H_{ad} \rightarrow H_2(g) \qquad Eq(4.3)$$

$$Ni(NH_3)_n^{2+} + 2e^- \rightarrow Ni\ (s) + nNH_3 \qquad Eq(4.4)$$

The deposition of Zn micro-platelets on top of the as-prepared Ni porous layer was performed under a -10 V power supply, at which the hydrogen evolution reaction occurs. The formation of Zn platelets was then affected by the hydrogen bubbling. The $Ni(OH)_2$ layer was created by a deposition procedure under a potential of -3 V on top of the porous Ni/Zn scaffold structure, following Equation 4.5 and 4.6:

$$NO_3^- + H_2O + 2e^- \rightarrow NO_2^- + OH^- \qquad Eq(4.5)$$

$$Ni^{2+} + 2OH^- \rightarrow Ni(OH)_2 \qquad Eq(4.6)$$

In this process, OH^- ions were generated under this potential associated with the reduction of NO_3^-. Then, the nickel hydroxides were produced through the OH^-/Ni^{2+} reaction. Accordingly, the Ni/Zn/$Ni(OH)_2$ hierarchal structure was generated from the precipitation of the $Ni(OH)_2$ layer.

4.3 Results and Discussion

The total mass of the deposition layer, by using -4 V and -10 V as the potential in fabricating the P-Ni (-4 V) and P-Ni (-10 V), respectively, ranged from 0.0048 to 0.0053 g and 0.0130 to 0.0135 g.

4.3.1 Physical Properties of Ni/$Ni(OH)_2$-Layered Structures

Scanning Electron Microscopy

Figure 4.3 shows the SEM images of the P-Ni, Zn@P-Ni, $Ni(OH)_2$@Zn@P-Ni, and Ni_{DHBT}. The morphology of the P-Ni (-10 V) and P-Ni (-4 V) are shown in Figure 4.3 (a) and (b), respectively. One can see that the average pore size and porosity on the two samples are very different. The average pore size in P-Ni (-4 V) is in the range of 8 to 12 μm. In P-Ni (-10 V), the average pore size is in the range of 10 to 15 μm with a porosity of 40 to 50/cm^2. Figure 4.3 (c) and (d) show the morphology of Zn@P-Ni (-10V) and Zn@P-Ni (-4 V), respectively. The electrodeposition of Zn on the Ni porous layer at -4 V and -10V forms Zn platelets on top of the Ni supporting layer. Figure 4.3 (e) and (f) show the morphology of $Ni(OH)_2$@Zn@P-Ni (-10 V) and $Ni(OH)_2$@Zn@P-Ni (-4 V), respectively.

The results show that once the $Ni(OH)_2$ layer was deposited on the surface of the Zn layer, a rough surface was created. Figure 4.3 (g) and (h) are the SEM images of the Ni_{DHBT} (-10 V) and Ni_{DHBT} (-4 V), respectively, which reveal the recreation of the smoothed surface by the $Ni(OH)_2$ deposition.

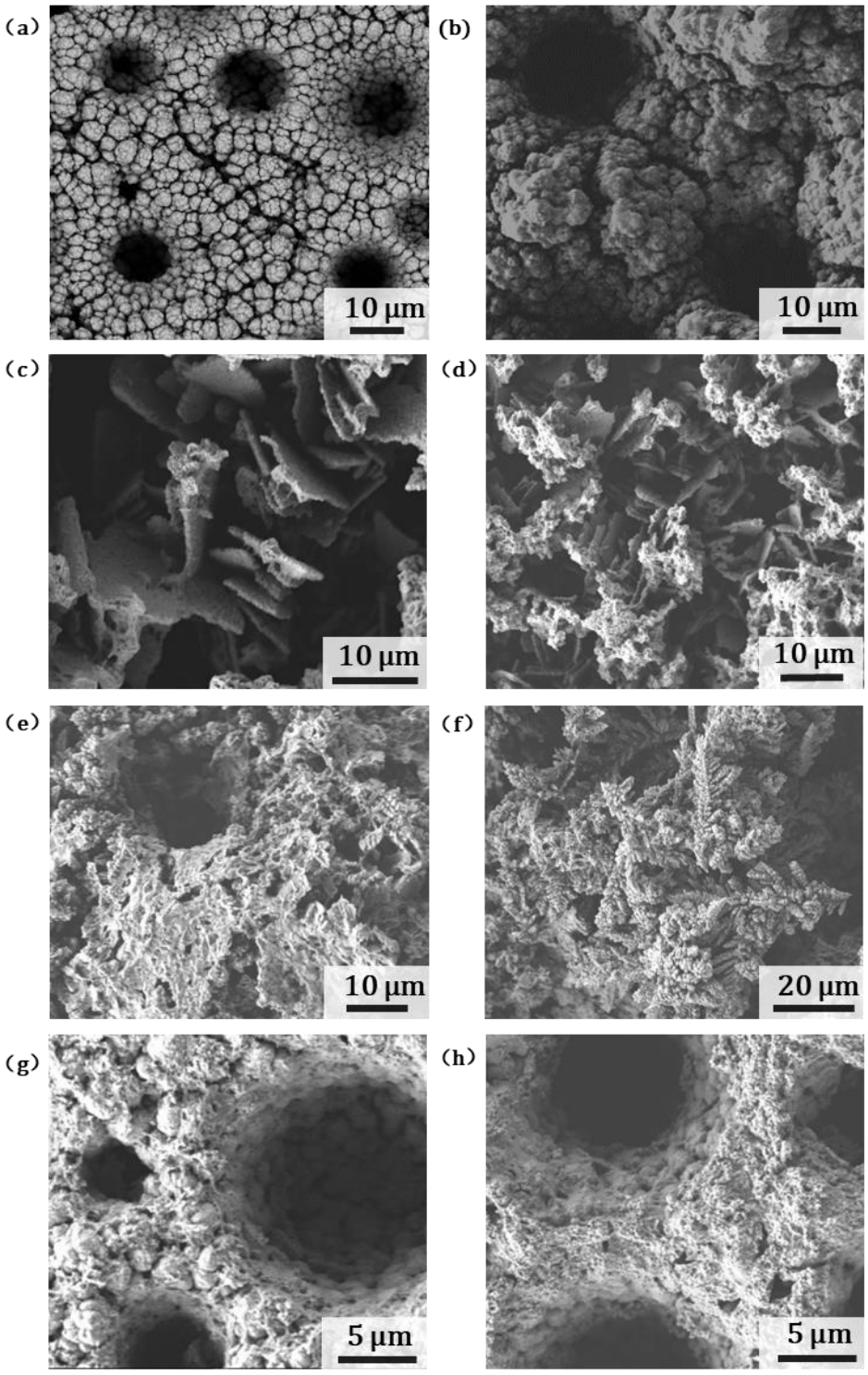

Figure 4.3 Surface morphology results from SEM measurement of (a) P-Ni (-10 V), (b) P-Ni (-4 V); (c) Zn@P-Ni (-10 V), (d) Zn@P-Ni (-4 V); (e) $Ni(OH)_2$@Zn@P-Ni (-10 V), (f) $Ni(OH)_2$@Zn@P-Ni (-4 V); and (g) Ni_{DHBT} (-10 V), and (h) Ni_{DHBT} (-4 V).

X-Ray Diffraction

The XRD pattern of the electrodeposited Ni_{DHBT} (-10 V) and Ni_{DHBT} (-4 V) catalysts are demonstrated in Figure 4.4 (a) and (b), respectively. The results show that both samples are Ni^0, as shown by the peaks at 44.532 °, 52.698 °, and 77.014 °. The characteristic peaks of α-$Ni(OH)_2$ were not observed in both samples. This is expected because α-$Ni(OH)_2$ is electrodeposited on a plain Ni substrate, and the latter is the main component in Ni_{DHBT} (-10 V) and Ni_{DHBT} (-4 V). In addition, no characteristic peaks of Zn crystal appeared in the XRD pattern, suggesting the successful removing of the Zn component in the etching process. The rear composition of oxygen was the proof of the tiny deposition amount of the $Ni(OH)_2$, which met the weak (003) α-$Ni(OH)_2$ peak evidence acquired from the XRD characterization.

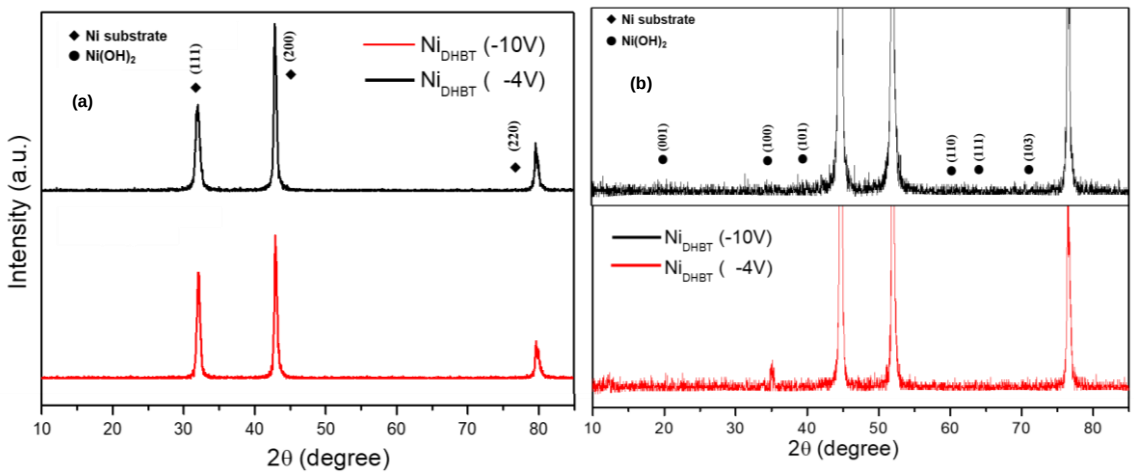

Figure 4.4 XRD patterns of Ni_{DHBT} (-10 V) and Ni_{DHBT} (-4 V) ([a] original, [b] zoomed in details).

4.3.2 Electrochemical Performance

ECSA and CV at the Cathodic Region

Figure 4.5 shows that the two Ni_{DHBT} catalysts electrodeposited under different potentials exhibited a huge difference in the performance under the cathodic region. This might have resulted from the H_2 bubbles generated at the two potentials. The initial deposited layer of Ni porous structure was conducted by the bubble-assisted method. The diameter of the generated H_2 bubbles under high voltage (-10 V) was much larger than that produced at low voltage (-4 V); additionally, the reaction rate under high voltage (-10 V) was much higher than that under low voltage (-4 V). Thus, more pores can be formed during the deposition at -10 V, and therefore, there are likely more active sites available

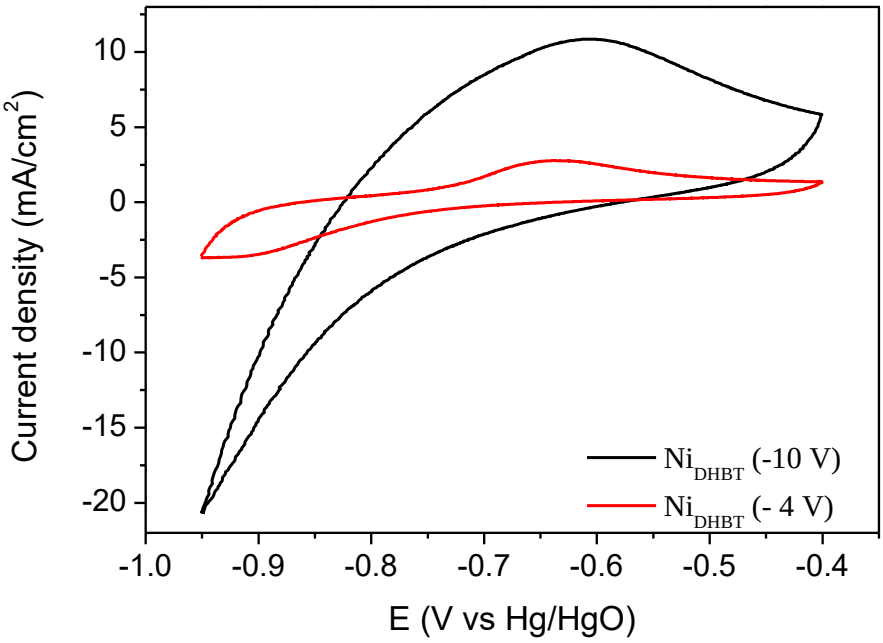

for the reaction, resulting in a large observed ECSA.

Figure 4.5 CV results of the Ni_{DHBT} (-10 V) and Ni_{DHBT} (-4 V) in the cathodic region. Scan rate = 50 mV·s^{-1}; electrolyte = 1 M KOH.

The OER activity of the Ni_{DHBT} (-10 V) and Ni_{DHBT} (-4 V) were measured. As shown

in Figure 4.6, the Ni_{DHBT} (-4 V) exhibits better OER activity than that of the Ni_{DHBT} (-10 V), with a lower overpotential at 277 mV compared to 299 mV at 10 $mA \cdot cm^{-2}$. However, the Tafel measurement showed that the Ni_{DHBT} (-4 V) displayed a much lower slope of the Ni_{DHBT} (-4 V) at 63.33 $mV \cdot dec^{-1}$ compared to 131.76 $mV \cdot dec^{-1}$ from Ni_{DHBT} (-10 V) (Figure 4.7). After the calculation, the exchange current density of the two materials reviewed in this chapter was $2.51 \times 10^{-7} A \cdot cm^{-2}$ and $1.58 \times 10^{-6} A \cdot cm^{-2}$. Compared to the calculated exchange current density, shown in Chapter 3, from the NMF materials, the value acquired from these Ni_{DHBT} materials was lower.

Electrochemical results are collected and exhibited in table 4.1. It is obviously to say that the NMF-O_2/H_2 shows the best performance among all the NMF materials which is recommended to have further modifications and studies.

Table 4.1 Collection of electrochemical results

Catalysts	**Tafel slope (**$mV.dec^{-1}$**)**	**Overpotential (**mV**)**	**Exchange current density (**$A \cdot cm^{-2}$**)**
Ni_{DHBT} (-4 V)	63.33	299	2.51×10^{-7}
Ni_{DHBT} (-10 V)	131.76	277	1.58×10^{-6}

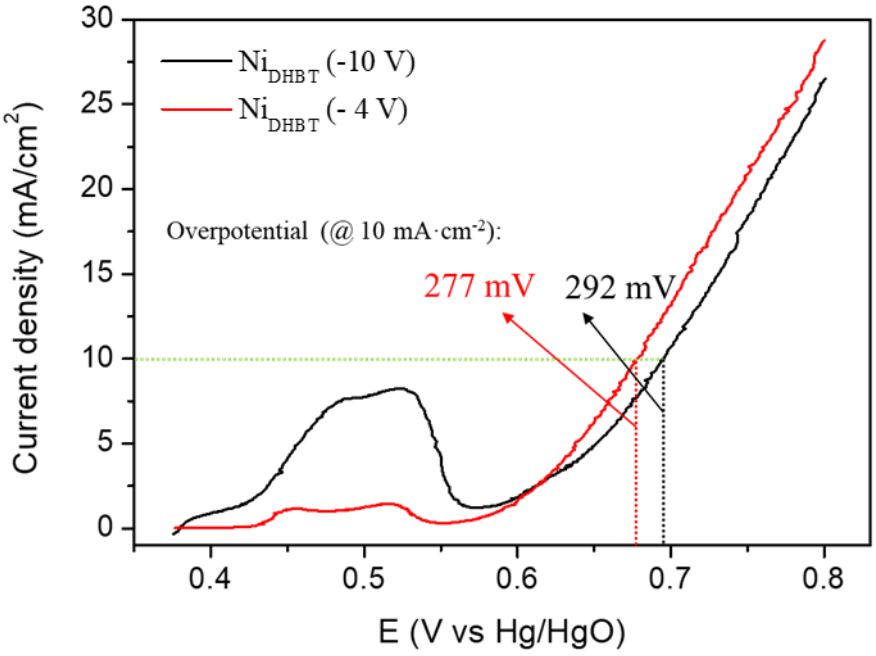

Figure 4.6 LSV results of the Ni$_{DHBT}$ (-10 V) and Ni$_{DHBT}$ (-4 V) in the anodic region. Scan rate = 1 mV·s^{-1}; electrolyte = 1 M KOH.

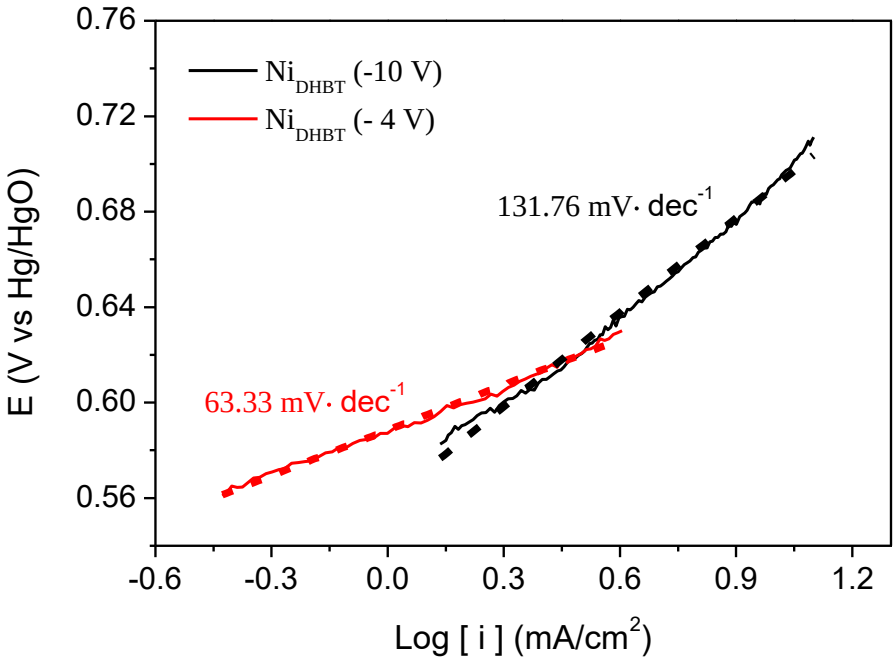

Figure 4.7 Tafel plots of the Ni$_{DHBT}$ (-10 V) and Ni$_{DHBT}$ (-4 V) in the anodic region. Scan rate = 1 mV·s^{-1}; electrolyte = 1 M KOH.

4.3.3 Effect of Etching Time

The effect of etching time driving the Zn removal process on the electrochemical performance of Ni_{DHBT} (-4 V) was studied. Figure 4.8 and 4.9 show the CVs obtained for the etched catalysts in the cathodic and anodic region, respectively. Their CV curves in the cathodic region are almost the same. In the anodic region, however, a higher limiting current density is delivered by Ni_{DHBT} (-4 V) with 1 hour of etching than by that etched for 4 hours, suggesting a higher OER activity with a short etching time.

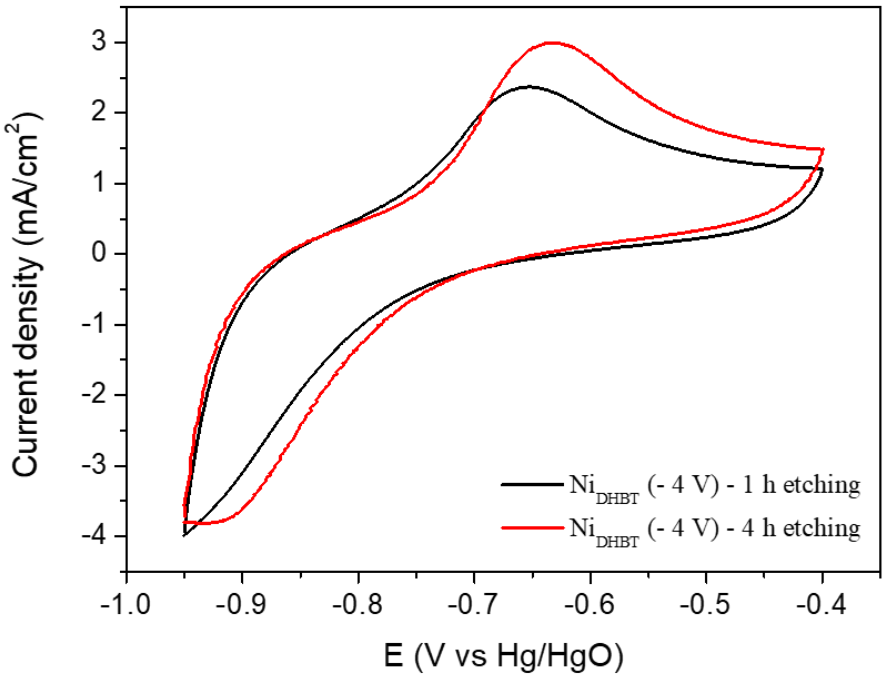

Figure 4.8 CV results of Ni_{DHBT} (-4 V) in different etching times (1 h and 4 h) in the cathodic region. Scan rate = 50 mV·s^{-1}; electrolyte = in 1 M KOH.

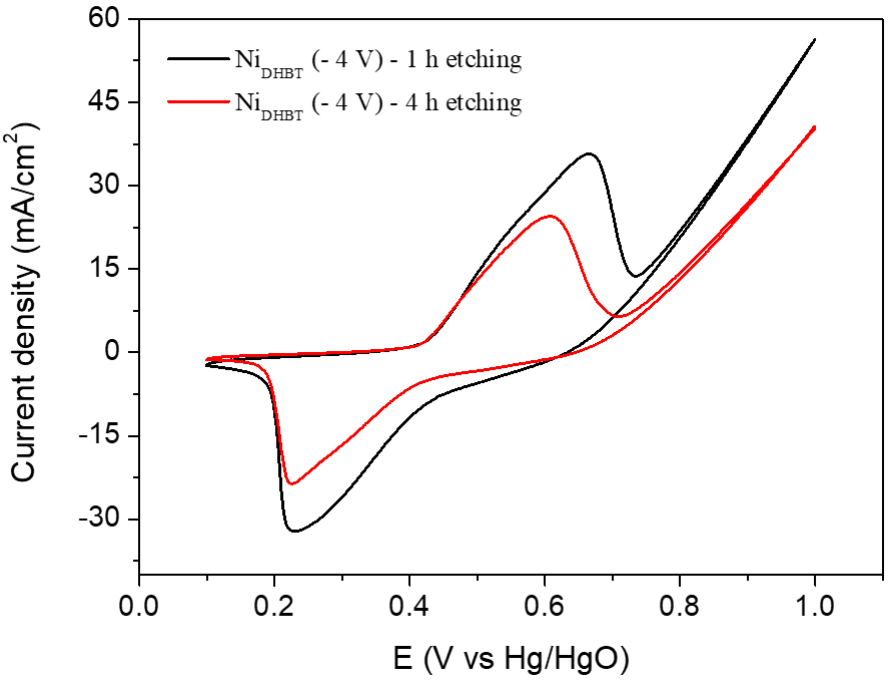

Figure 4.9 CV results of Ni_{DHBT} (-4 V) in different etching times (1 h and 4 h) in the anodic region. Scan rate = 50 mV·s^{-1}; electrolyte = 1 M KOH.

To further confirm the results, the operating potentials required for the two catalysts to deliver a 10.0 mA·cm^{-2} current density were also compared using LSV analysis. The Ni_{DHBT} (-4 V) etched for 1 hour reached a current density of 10.0 mA·cm^{-2} at 0.73 V, lower than that etched for 4 hours (0.77 V) (Figure 4.10). The lower potential obtained for Ni_{DHBT} (-4 V)-1h verified its higher OER activity than that of Ni_{DHBT} (-4 V)-4h, suggesting that a short etching time is preferred.

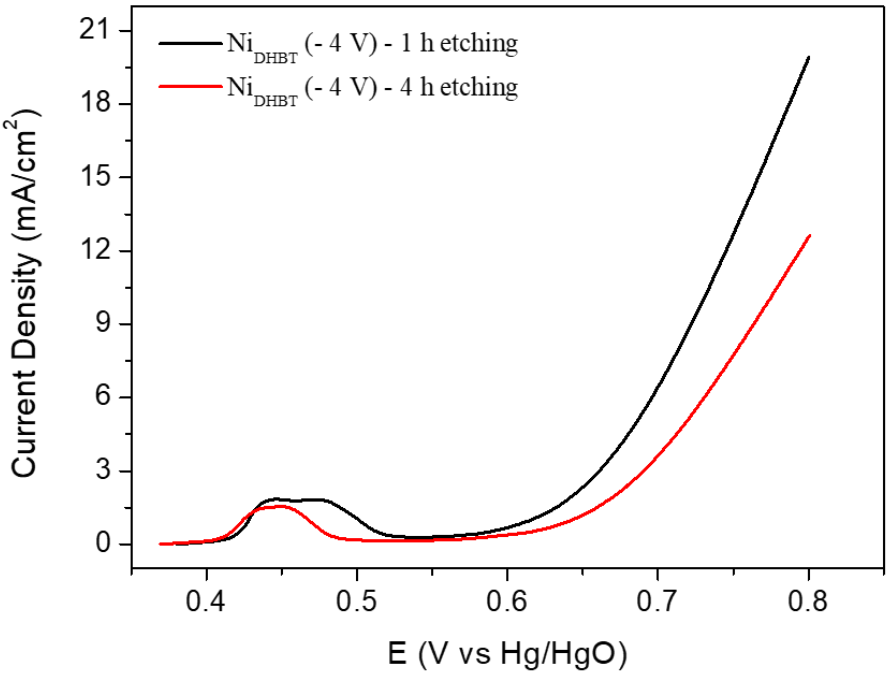

Figure 4.10 LSV results of Ni$_{DHBT}$ (-4 V) in different etching times (1 h and 4 h). Scan rate = 1 mV·s^{-1}; electrolyte = 1 M KOH.

4.3.4 Evaluation of the Existence of Zn Deposition

Physical Properties of Structures with/without Zn Layer Deposition

Figure 4.11 is the SEM micrographs of the P-Ni (-4 V) and Ni$_{DHBT}$ (-4 V) catalysts that were obtained with (w-Zn) and without (w/o-Zn) Zn deposition. It can be seen from Figure 4.11 (a–c) that P-Ni (-4 V) presents a three-dimensional flower-like morphology. In Ni$_{DHBT}$ (-4 V) w/o-Zn, the morphology still retains the characteristics of P-Ni (-4 V). However, the size of the foam particle is smaller than that of P-Ni (-4 V) (Figure 4.11 [b]). Upon Zn deposition, a nanowire-like structure was observed on the surface of the resulting Ni$_{DHBT}$ (-4 V) w-Zn foam catalyst (Figure 4.11 [d]).

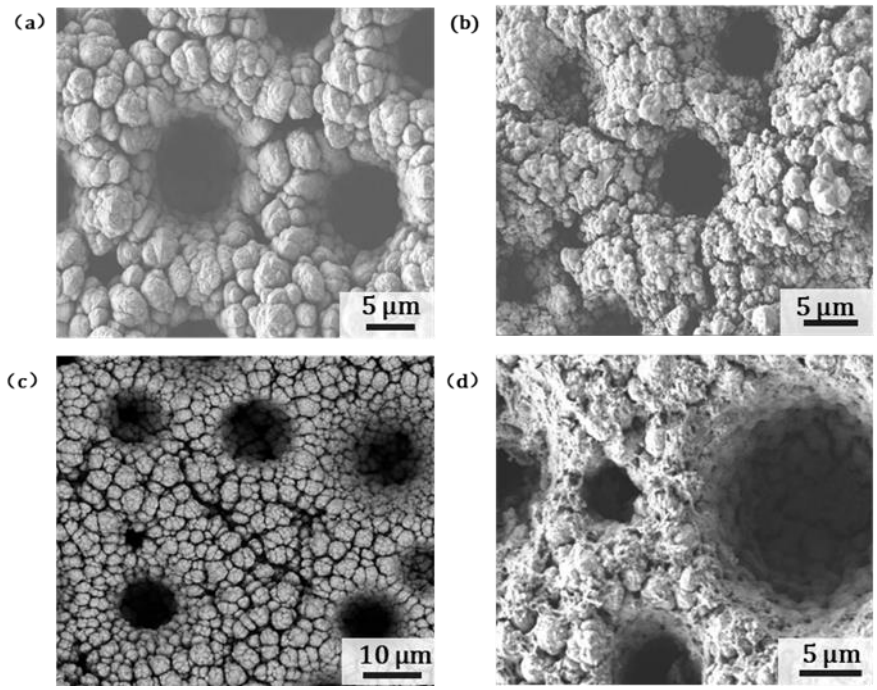

Figure 4.11 SEM images of (a, c) P-Ni (-4 V), (b) Ni_{DHBT} (-4 V) w/o-Zn，(d) Ni_{DHBT} (-4 V) w-Zn.

Electrochemical Performance of Structures with/without Zn Layer Deposition

Figure 4.12 shows the electrochemical performance of the Ni_{DHBT} material with and without Zn deposition compared to the plain Ni substrate. From the results, the highest current density that the Ni_{DHBT} without Zn deposition can achieve is higher than that of Ni_{DHBT} with Zn deposition. Based on the conclusion from Section 4.3.3, which shorter etching time resulted to higher current density. One hypothesis could be that the Zn residue has side-reactions that contribute to the enhancing of OER. The results from this section show a completely reversed conclusion about the existence of Zn and the deposition of a

Zn layer compared to the conclusion from Section 4.3.3.

Figure 4.12 CV results of Ni_{DHBT} -with Zn, Ni_{DHBT} -w/o Zn, and plain Ni substrate. Scan rate = 50 $mV \cdot s^{-1}$; electrolyte = 1 M KOH.

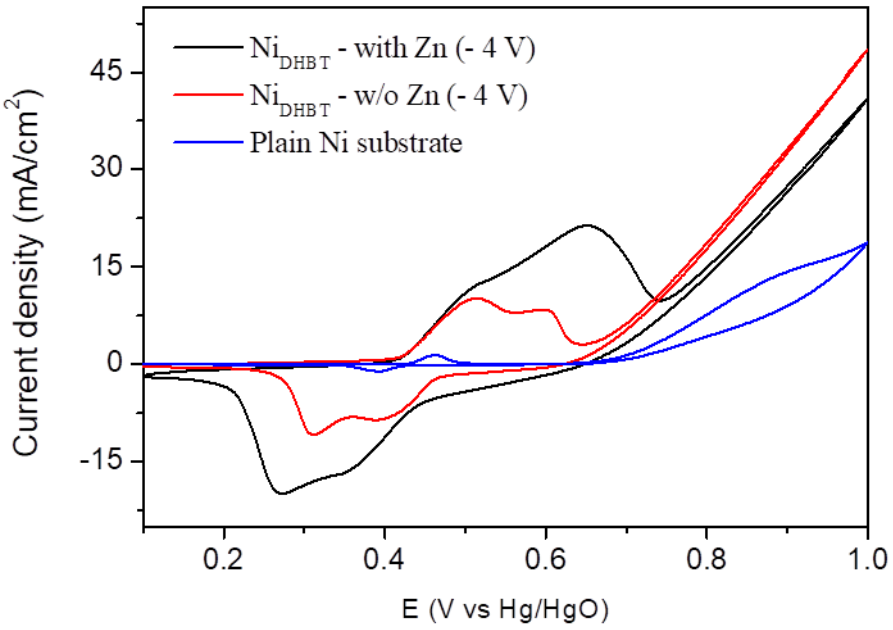

4.4 Summary

In this study, a honeycomb-like 3D porous Ni/$Ni(OH)_2$-layered Ni_{DHBT} catalyst was successfully fabricated through a dynamic hydrogen bubble templating method followed by a chemical etching treatment. Specifically, a P-Ni sample was first obtained after the bubble-assisted electrodeposition treatment of a plain Ni plate, which exhibited a honeycomb-like pores distribution. On the basis of P-Ni, the deposition of Zn platelets and further construction of $Ni(OH)_2$ were performed, creating a multiple-layered structure on top of the flower-like porous Ni substrate. Once Zn was removed, $Ni(OH)_2$ covered the meso-pores of the Ni_{DHBT} surface.

The electrochemical performance of Ni_{DHBT} was investigated by CVs, LSV, and Tafel measurements. The results show that, due to the bubble size and quantity, a higher ECSA was generated at the high potential. In the catalysis of OER, both of the Ni_{DHBT} (-4 V) and Ni_{DHBT} (-10 V) materials showed a relatively low overpotential to reach the current density of 10 $mA \cdot cm^{-2}$. The Ni_{DHBT} (-4 V) displayed a better result with an overpotential of 277 mV and a Tafel slope of 63.33 $mV \cdot dec^{-1}$. That is, Ni_{DHBT} (-4 V) was the material optimized toward OER.

Reference

[1]. Yu, J., Cao, Q., Li, Y., Long, X., Yang, S., Clark, J. K., Nakabayashi, M., Shibata, N., & Delaunay, J. J. (2019). Defect-Rich NiCeOx Electrocatalyst with Ultrahigh Stability and Low Overpotential for Water Oxidation [Rapid-communication]. ACS Catalysis, 9(2), 1605–1611.

[2]. Wang, D., Watanabe, F., & Zhao, W. (2016). One-pot growth of 3D reduced graphene oxide foams embedded with NiFe oxide nanocatalysts for oxygen evolution reaction. Journal of the Electrochemical Society, 163(11), F3158–F3163.

[3]. Liu, G., Li, J., Fu, J., Jiang, G., Lui, G., Luo, D., Deng, Y. P., Zhang, J., Cano, Z. P., Yu, A., Su, D., Bai, Z., Yang, L., & Chen, Z. (2019). An Oxygen-Vacancy-Rich Semiconductor-Supported Bifunctional Catalyst for Efficient and Stable Zinc–Air Batteries. Advanced Materials, 31(6), 1–7.

[4]. Li, J. C., Hou, P. X., Zhao, S. Y., Liu, C., Tang, D. M., Cheng, M., Zhang, F., & Cheng, H. M. (2016). A 3D bi-functional porous N-doped carbon microtube sponge electrocatalyst for oxygen reduction and oxygen evolution reactions. Energy and Environmental Science, 9(10), 3079–3084.

[5]. Lui, G., Li, G., Wang, X., Jiang, G., Lin, E., Fowler, M., Yu, A., & Chen, Z. (2016). Flexible, three-dimensional ordered macroporous TiO2 electrode with enhanced electrode–electrolyte interaction in high-power Li-ion batteries. Nano Energy, 24, 72–77.

[6]. Xiong, Q. Q., Qin, H. Y., Chi, H. Z., & Ji, Z. G. (2016). Synthesis of porous nickel networks supported metal oxide nanowire arrays as binder-free anode for lithium-ion batteries. Journal of Alloys and Compounds, 685, 15–21.

[7]. Hao, M., Charbonneau, V., Fomena, N. N., Gaudet, J., Bruce, D. R., Garbarino, S., Harrington, D. A., & Guay, D. (2019). Hydrogen Bubble Templating of Fractal Ni Catalysts for Water Oxidation in Alkaline Media [Research-article]. ACS Applied Energy Materials, 2(8), 5734–5743.

[8]. Aghazadeh, M., Ghaemi, M., Sabour, B., & Dalvand, S. (2014). Electrochemical preparation of α-$Ni(OH)_2$ ultrafine nanoparticles for high-performance supercapacitors. Journal of Solid State Electrochemistry, 18(6), 1569–1584.

[9]. Xiao, M., Tian, Y., Yan, Y., Feng, K., & Miao, Y. (2015). Electrodeposition of $Ni(OH)_2$/NiOOH in the Presence of Urea for the Improved Oxygen Evolution. Electrochimica Acta, 164, 196–202.

[10]. Rao, Y., Wang, Y., Ning, H., Li, P., & Wu, M. (2016). Hydrotalcite-like $Ni(OH)_2$ Nanosheets in Situ Grown on Nickel Foam for Overall Water Splitting. ACS Applied Materials and Interfaces, 8(49), 33601–33607.

[11]. Chiroptical, A. G., & One, C. (2013). Electronic Supplementary Information (ESI). c, 1–5.

[12]. Liu, Q., Xie, L., Liu, Z., Du, G., Asiri, A. M., & Sun, X. (2017). A Zn-doped Ni_3S_2 nanosheet array as a high-performance electrochemical water oxidation catalyst in alkaline solution. Chemical Communications, 53(92), 12446–12449.

[13]. Wang, S., Nai, J., Yang, S., & Guo, L. (2015). Synthesis of Amorphous Ni-Zn Double Hydroxide Nanocages with Excellent Electrocatalytic Activity toward Oxygen Evolution Reaction. ChemSusChem, 8(19), 3191.

[14]. Wang, S., Nai, J., Yang, S., & Guo, L. (2015). Synthesis of Amorphous Ni-Zn Double Hydroxide Nanocages with Excellent Electrocatalytic Activity toward Oxygen Evolution Reaction. ChemSusChem, 8(19), 3191.

[15]. Dong, Y., Zhang, P., Kou, Y., Yang, Z., Li, Y., & Sun, X. (2015). A First-Principles Study of Oxygen Formation Over NiFe-Layered Double Hydroxides Surface. Catalysis Letters, 145(8), 1541–1548.

[16]. Feng, L., Li, A., Li, Y., Liu, J., Wang, L., Huang, L., Wang, Y., & Ge, X. (2017). A Highly Active CoFe Layered Double Hydroxide for Water Splitting. ChemPlusChem, 82(3), 483–488.

[17]. Geng, X., Liang, W., & Podlaha, E. J. (2017). A methodology to electrochemically fabricate Fe-Ni-Co nanotips. Journal of the Electrochemical Society, 164(4), D218–

D224.

[18]. Yanai, T., Azuma, K., Eguchi, K., Watanabe, Y., Ohgai, T., Nakano, M., & Fukunaga, H. (2016). Effects of annealing and pulse plating on soft magnetic properties of electroplated Fe-Ni films. AIP Advances, 6(5).

[19]. Bento, F. R., & Mascaro, L. H. (2006). Electrocrystallisation of Fe-Ni alloys from chloride electrolytes. Surface and Coatings Technology, 201(3–4), 1752–1756.

[20]. Yang, X., Duan, X., & Yuan, H. (2012). Electrodeposition of iron-enriched nanocrystalline Fe-Ni alloy foil from chloride-sulfate solutions. Anti-Corrosion Methods and Materials, 59(1), 18–22.

Chapter 5 - Promotion of 3D Ni Materials by Iron Oxides for OER

Based on the porous NMF-O_2/H_2 foam and Ni_{DHBT} catalysts catalysts explained in Chapter 3 and 4, a FeO_x deposition catalyst design strategy was proposed to study the effect of FeO_x on the activity of Ni foam-based catalysts. The morphology and electrochemical properties of these deposited catalysts, referred to as Fe@NMF-O_2 and Fe@Ni_{DHBT}, were investigated. The results show that the addition of small quantities of FeO_x significantly improve the OER activity of the Ni porous catalysts. The optimized Fe@Ni_{DHBT} catalyst is Fe@Ni_{DHBT} (-4 V) (5:95), which shows the highest OER activity with an overpotential of ~247 mV at a current density of 10 $mA{\cdot}cm^{-2}$. This work sheds light on using a facile FeO_x deposition method as a promising strategy to design efficient Ni-based OER electrocatalysts.

5.1 Introduction

The OER is the key half-reaction and bottleneck in water splitting. As discussed above, the rate of OER is hindered by its slow reaction kinetics. Due to its earth-abundant nature and high reaction activity toward OER, Ni-based metals have attracted extensive attention. Recently, it was reported that incorporation of heteroatom components into Ni (hydro)oxides can largely enhance OER activity in alkaline solution. The improved

electrochemical performance is usually attributed to synergistic metal-metal interactions. [1, 2]

Among the heteroatoms, the introduction of Fe into Ni-based materials is a widely reported strategy to further improve OER performance. For example, many nickel-iron oxides ($NiFeO_x$) have been developed as efficient OER catalysts in alkaline solution, and these $NiFeO_x$-based catalysts usually require overpotentials of 300 to 400 mV to deliver a current density of 10 $mA{\cdot}cm^{-2}$ [3,4]. In the study by Xing et al. [5], a highly efficient 3D, porous nickel-iron phosphates electrocatalyst was developed via a simple electrodeposition method. In 1 M KOH, the Fe-Ni catalyst presents excellent OER catalytic activity; it requires overpotentials of 204 mV to generate 20 mA cm^{-2}. In another study, a high-performance oxygen electrode toward water oxidation was fabricated by electrodepositing the mesoporous nickel-iron composite nanosheets onto macroporous nickel foam substrates [6].

Following the same strategy, on the basis of the porous NMF-O_2/H_2 foam and Ni_{DHBT} catalysts synthesized in Chapter 3 and 4, we further deposited FeO_x colloid onto the surface of NMF-O_2/H_2 and Ni_{DHBT}. The resulting catalysts are referred to as FeO_x-NMF-O_2/H_2 foam and FeO_x-Ni_{DHBT}, respectively. Electrochemical analysis shows that the OER activity of Ni foam-based catalysts is significantly promoted by the introduction of FeO_x. Additionally, the effect of FeO_x loading on the OER performance of these catalysts was studied. All the electrochemical results were referred to the Hg/HgO as the reference

electrode.

5.2 Experimental Procedure

5.2.1 Synthesis of FeO_x colloid

The Fe colloid was prepared by following a published method from LEE group by adding 0.72 g of $Fe(NO_3)_3$ (99.999%, Sigma Aldrich) and 0.25 mol of NaOH (98%, Fisher Scientific) into 50 mL of ethylene glycol (EG) (99.999%, Sigma Aldrich). The solution was stirred for 30 minutes at room temperature. The solution was then refluxed at 160 ℃ for 3 hours. The color of the colloid product was light brown, implying the dominating species was iron oxide (FeO_2). [7]

5.2.2 Synthesis of Fe@NMF-O_2/H_2 Foam

The Fe@NMF-O_2/H_2 foam was fabricated by depositing FeO_x particles onto the surface of NMF-O_2/H_2 foam with an agitation procedure with the shaker. With the effect of the loading amount of FeO_x taken into consideration, a different FeO_x-Ni mass ratio was considered when preparing the solution (e.g. 99% – 1%, 95% – 5%, 90% – 10%, and 80% – 20%) and was placed into a 10 mL vial. Then, 3 mL ethanol (99.999%, Fisher Scientific) was added into the vial. During the synthesis, the shaker was maintained at 300 rpm under 50℃ for three days to ensure a sufficient mixing time between Fe colloids and NMF. Once the synthesis was compete, the solution was then rinsed with deionized water and ethanol five times each to remove ethylene glycol as well as the upper suspension, which contained

the unreacted Fe particles. The products were air-dried in an oven under 60°C overnight.

5.2.3 Synthesis of Fe@Ni$_{DHBT}$ Materials

The Fe@Ni$_{DHBT}$ catalyst was prepared by physically depositing FeO_x ink on nanostructured Ni. To prepare the diluted FeO_x ink solution, 5 mL of as-synthesized FeOx colloidal solution was transferred into a centrifuge tube and rinsed with deionized water (18.5mΩ) and ethanol (≥99.8%, Fisher Scientific) several times to completely remove the residual ethylene glycol. The solution was then centrifuged (Allegra X-30 Series, Beckman Coulter) at a rotating speed of 10,000 rpm for five minutes in order to acquire FeO_x powder. The FeO_x ink (0.25 M) was prepared by adding 6 mg FeO_x powder, 1.0 mL deionized water, 200 μL isopropanol, and 100 μL Nafion solution. The Fe@Ni$_{DHBT}$ catalysts were synthesized by dropping FeO_x ink on top of the Ni$_{DHBT}$ at a Ni:Fe mass ratio of 99:5.

5.2.4 Physical and Electrochemical Characterizations

The surface morphology, crystal structure, and the electrochemical properties of the catalysts were studied using SEM, XRD and CA, CV, and LSV analysis. Details can be found in Chapter 3.2.

Microwave plasma atomic emission spectroscopy (MP-AES, 4210 MP-AES, Agilent) elemental composition analysis was conducted by Dr. Nimal da Silva in the Geochemistry Lab in the Department of Earth and Environmental Sciences at the University of Ottawa.

5.3 Results and Discussion

5.3.1 Physical Properties of Fe@NMF-O_2/H_2

The physiochemical and electrochemical characterizations were only performed with Fe@NMF-O_2/H_2 (5:95) since the electrochemical performances were relatively good compared to the rest of the Fe-NMF materials. This is because the catalysts with lower designed Fe loading amount showed much less activity as well as because the higher designed Fe loading amount materials did not show much higher real loading Fe amount and catalytic promotion.

Scanning Electron Microscopy

Figure 5.1 shows the SEM images of NMF-O_2/H_2 (Figure 5.1 [a, b]) and Fe@ NMF-O_2/H_2 (5:95) (Figure 5.1 [c, d]). NMF-O_2/H_2 is the supporting material, and after FeO_x deposition, the cross-linked wire and hollow structure was well-preserved in the resulting Fe@NMF (5:95). Figure 5.1 (c, d) shows that, compared to NMF-O_2/H_2, the micro holes on the wires of Fe@ NMF-O_2/H_2 were partially covered by FeO_x particles resulting in an increase of its surface roughness. A quick EDS mapping was carried out to obtain the element information soon after the surface structure detection. From EDS mapping, only basic Ni, C, and O were found in the material. A hypothesis was made that the loading amount of the Fe meso-particles was too small so the particles could not be clearly detected with this method. However, based on the electrochemical results, the significant promotion proved that changes appeared after the mixing procedure of FeO_x particles and Ni support. Thus, an MP-AES was applied to give further understandings of this material.

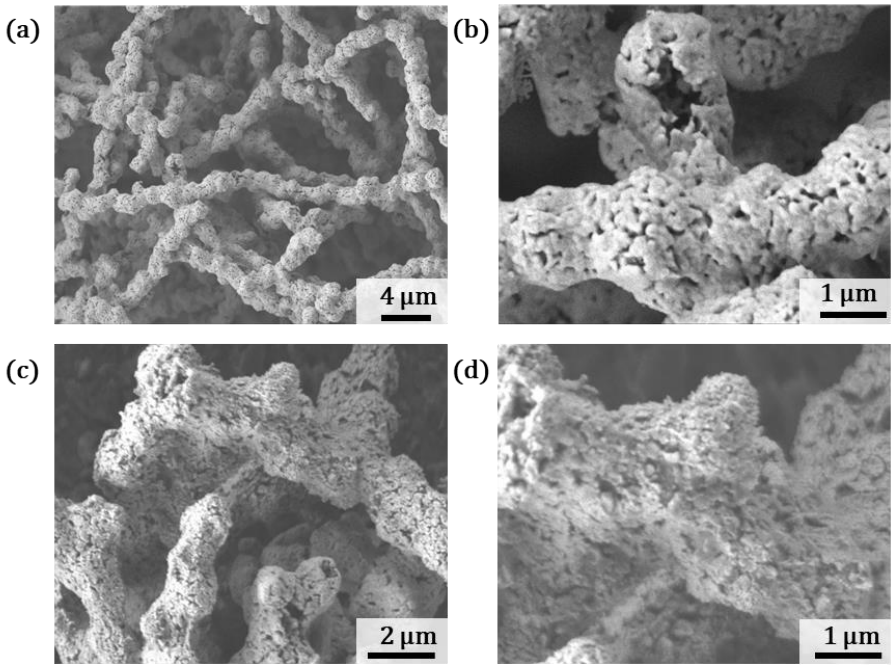

Figure 5.1 SEM images of (a, b) NMF-O_2/H_2 and (c, d) Fe@NMF-O_2/H_2 (5:95).

MP-AES Characterization

MP-AES measurements were used to determine the elemental ratio of the Fe@ NMF-O_2/H_2 (5:95). Table 5.1 shows that the total amount of Ni and Fe determined by MP-AES was 965.32 mg/g and 15.230 mg/g, respectively, which corresponds to a Ni:Fe ratio of 98.45:1.55.

Table 5.1 MP-AES characterization of elements composition of Fe@ NMF-O_2/H_2 (5:95).

	Fe	Ni
Limit of Detection (µg/g)	**0.007**	**0.007**
Powder mass (mg/g)	**15.23**	**965.32**
Concentration (%)	**1.52**	**96.53**

5.3.2 Physical Properties of Fe@Ni$_{DHBT}$

SEM Characterization

Figure 5.2 (a) shows the SEM image of Ni$_{DHBT}$ (-4 V) that was used to deposit FeO_x nanoparticles. The morphology of FeO_x-Ni$_{DHBT}$ (-4 V) (5:95), referred to as Fe@Ni$_{DHBT}$ (-4 V) (5:95), are demonstrated in Figure 5.2 (b). A comparison of the two images shows that, after FeO_x deposition, the pores on the Ni$_{DHBT}$ (-4 V) support surface were partially covered with a cracked shell structure. This phenomenon was resulted by the shrinkage of the $Ni(OH)_2$ layer during the loading procedure of FeO_x particles.

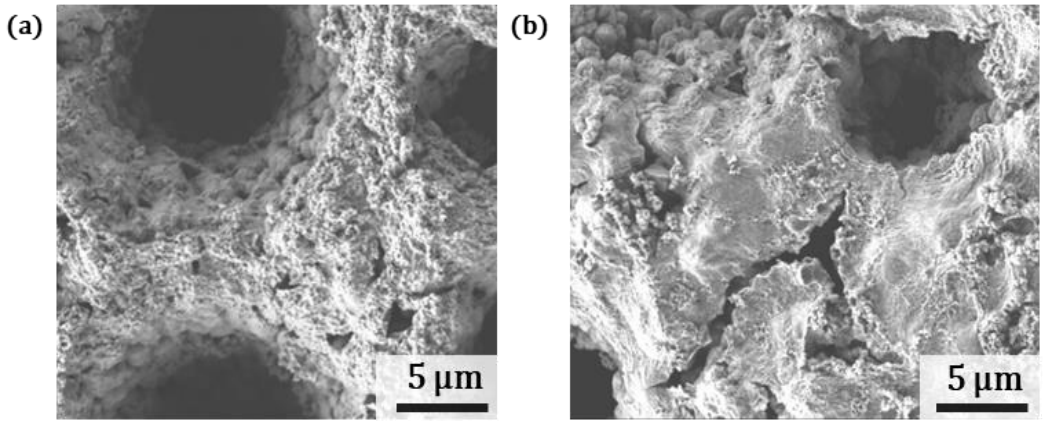

Figure 5.2 SEM images of (a) Ni$_{DHBT}$ (-4 V) and (b) Fe@Ni$_{DHBT}$ (-4 V) (5:95).

MP-AES Characterization

Table 5.2 summarizes the elemental composition of Fe@Ni$_{DHBT}$ (-4 V) (5:95), which was measured using MP-AES. The results show that the composite consists of 15.230 mg/g Fe and 965.32 µg/g Ni. This corresponds to a Ni:Fe ratio of 98.44:1.56.

Table 5.2 MP-AES characterization of elemental composition of Fe@Ni_{DHBT} (-4 V) (5:95).

	Fe	Ni	Zn
Limit of Detection (μg/g)	0.007	0.007	0.031
Powder mass (mg/g)	8300	965.32	0.246
Concentration (%)	0.830	89.9	0.025

5.3.3 Electrochemical Performance of Fe@NMF-O_2/H_2

The catalyst was further evaluated for its ability to catalyze the OER by recording anodic LSVs between 0.35 to 0.80 V vs Hg/HgO (Figure 5.3). The results show that, compared to that of NMF-O_2/H_2, Fe@NMF-O_2/H_2 (5:95) displayed a much higher anodic current, indicating its terrific catalytic activity in electrocatalyzing the OER. The overpotential of the catalysts, defined as the potential to reach a current density of 10 $mAcm^{-2}$, is about 262 mV, which also showed a huge promotion compared to that (364 mV) of the NMF-O_2/H_2.

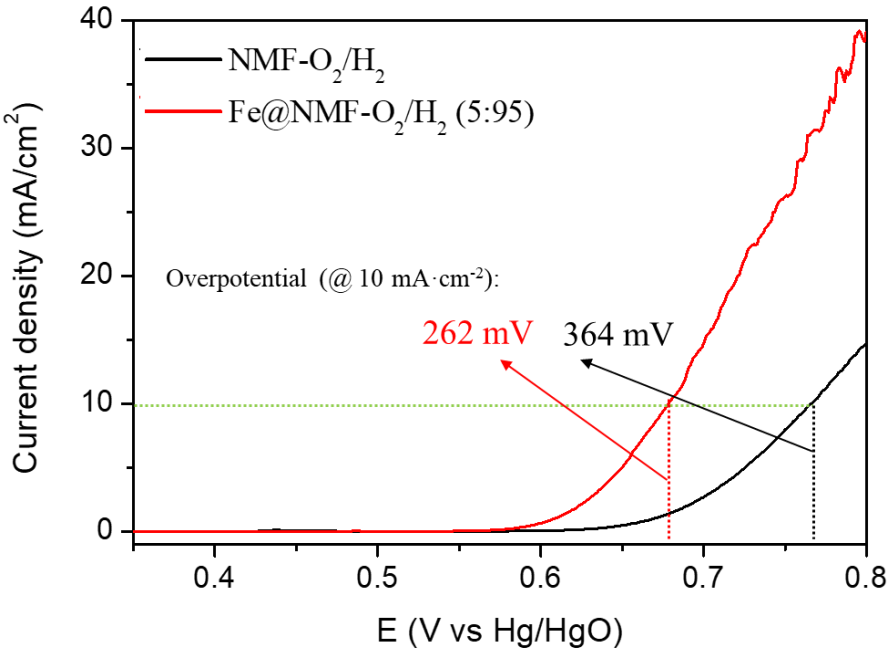

Figure 5.3 LSV results of NMF-O_2/H_2 and Fe@NMF-O_2/H_2 (5:95). Scan rate = 1 mV·s^{-1}; electrolyte = 1 M KOH.

The enhanced activity of Fe@NMF-O_2/H_2 (5:95) is also consistent with what is revealed by its Tafel plot (Figure 5.4). Results of Tafel analysis indicate that Fe@NMF-O_2/H_2 (5:95) exhibited a lower Tafel slope (45.40 mV dec^{-1}) than that of NMF-O_2/H_2 (61.55 mV dec^{-1}), suggesting an intrinsically higher OER kinetics of Fe@NMF-O_2/H_2 (5:95). After the calculation, the exchange current density of the Fe@NMF-O_2/H_2 material in this chapter was 1.64×10^{-7}A cm^{-2}. Compared with the calculated exchange current density (see Chapter 3) of the NMF-O_2/H_2 materials (7.69×10^{-5}A cm^{-2}), the value acquired from these Ni_{DHBT} materials was much lower.

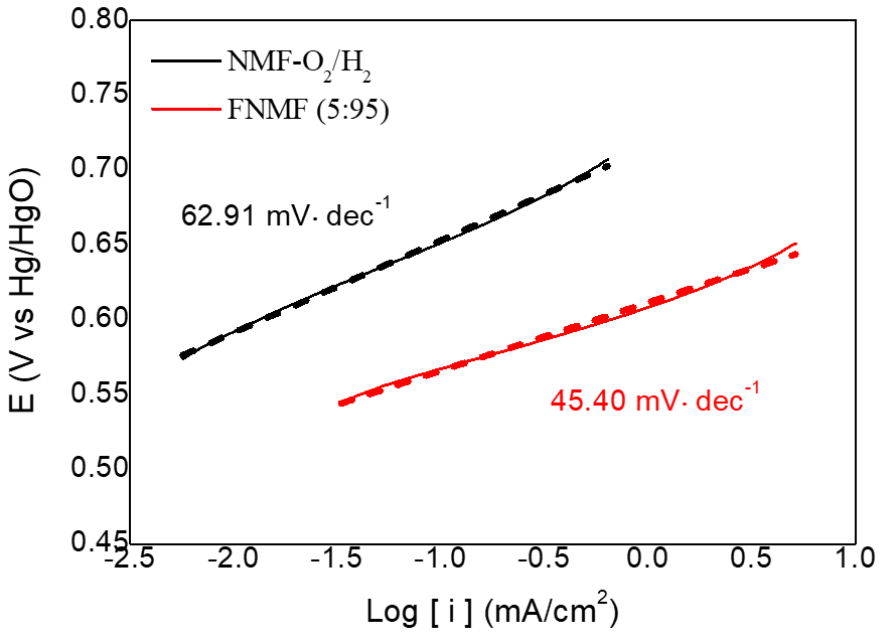

Figure 5.4 Tafel plots of the NMF-O_2/H_2 and Fe@NMF-O_2/H_2 (5:95). Scan rate = 1 mV·s^{-1}; electrolyte = 1 M KOH.

Furthermore, the electrochemical stability of Fe@NMF-O_2/H_2 (5:95) was studied by recording the current-over-time curve at an applied potential of E = 0.7 V (Figure 5.5). The analysis shows that, after 1 hour of continuous operation, the current delivered by the electrode showed negligible loss, indicating that it has good durability toward OER.

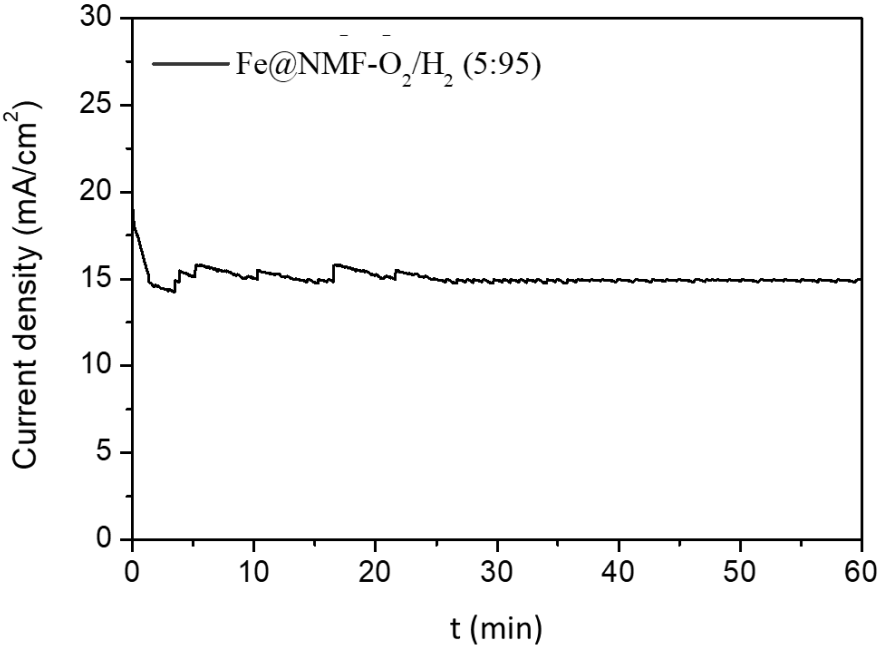

Figure 5.5 Stability test of Fe@NMF-O_2/H_2 (5:95), under E=0.7 V (vs Hg/HgO) for 1 hour in 1 M KOH.

The electrochemical performance of these catalysts was studied using CV and LSV analysis, respectively (Figure 5.6 and 5.7). In the LSV analysis, the activity of these catalysts can also be evaluated by comparing the operating potentials required to achieve a current density of 10 mA/cm^2. For example, the Fe@NMF-O_2/H_2 (20:80) displays a relatively lower potential (0.67 V) compared to Fe@NMF-O_2/H_2 (5:95) (0.68 V), Fe@NMF-O_2/H_2 (10:90) (0.68 V), and Fe@NMF-O_2/H_2 (20:80) (0.72 V) (see Figure 5.8). In other words, Fe@NMF-O_2/H_2 with a Ni-Fe ratio of 80:20 exhibits the best activity. However, considering the close results and unnecessary waste of FeO_x particles, Fe@NMF-O_2/H_2 (5:95) was a better choice.

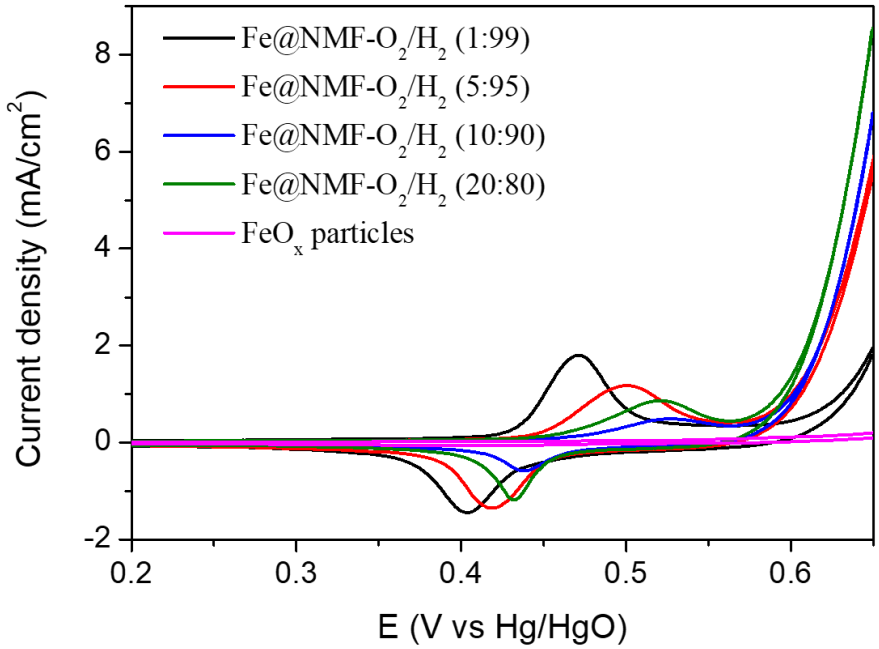

Figure 5.6 CV results of Fe@NMF-O_2/H_2 developed with different Ni-Fe ratios (99:1, 95:5, 90:10, 80:20). Scan rate = 50 mV·s^{-1}; electrolyte = 1 M KOH.

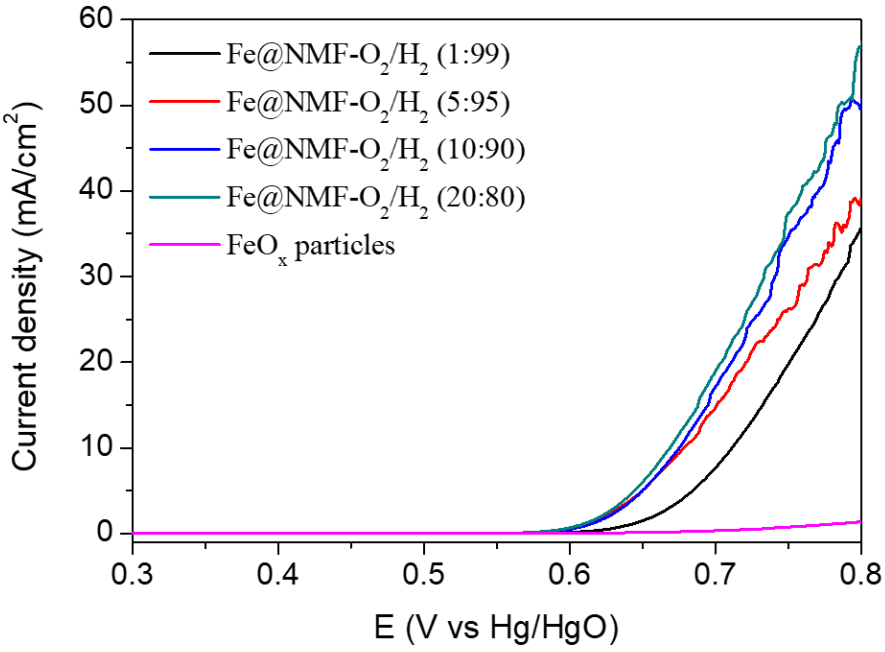

Figure 5.7 LSV results of Fe@NMF-O_2/H_2 developed with different Ni-Fe ratio (99:1, 95:5, 90:10, 80:20). Scan rate = 1 mV·s^{-1}; electrolyte = 1 M KOH.

The catalytic kinetics of the Fe@NMF-O_2/H_2 catalyst for OER was also examined and compared by Tafel plots. Tafel slope results are showed in Table 5.3.

Table 5.3 Tafel slopes for Fe@NMF-O_2/H_2 materials

	Fe@NMF-O_2/H_2				FeO_x particles
Ratio (Ni:Fe)	99:1	95:5	90:10	80:20	×
Tafel Slope ($mV \cdot dec^{-1}$)	52.30	41.90	40.88	40.56	117.36

The results are consistent with those observed in the LSV curve, indicating a higher OER kinetics of Fe@NMF-O_2/H_2 (20:80). However, considering the lesser promotion and higher cost of preparing the Fe@NMF-O_2/H_2 (20:80), Fe@NMF-O_2/H_2 (5:95) was relatively the best material.

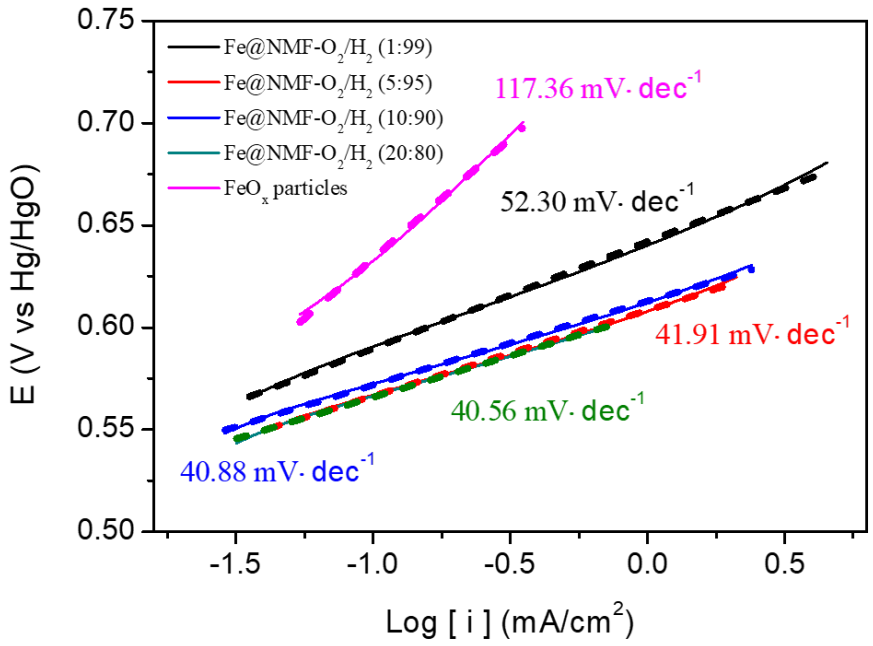

Figure 5.8 Tafel plots of the Fe@NMF-O_2/H_2 catalyst from different ratio of Ni:Fe ratio (99:1, 95:5, 90:10, 80:20) and FeO_x particles. Scan rate = 1 $mV \cdot s^{-1}$; electrolyte = 1 M KOH.

5.3.4 Electrochemical Performances of Fe@Ni$_{DHBT}$ (-4 V) Materials

Figure 5.9 presents the LSV curves of Fe@Ni$_{DHBT}$ (-4 V) measured in 1 M KOH solution. The results show that Fe@Ni$_{DHBT}$ (-4 V) exhibits the highest activity among these catalysts. When a current density of 10 mA cm^{-2} is generated, Fe@Ni$_{DHBT}$ (-4 V) exhibits an OER overpotential of ~247 mV, much lower than that of Ni$_{DHBT}$ (-4 V) and Ni$_{DHBT}$ (-10 V). The greatly enhanced OER activity of Fe@Ni$_{DHBT}$ (-4 V) suggests that Fe is the active component for OER.

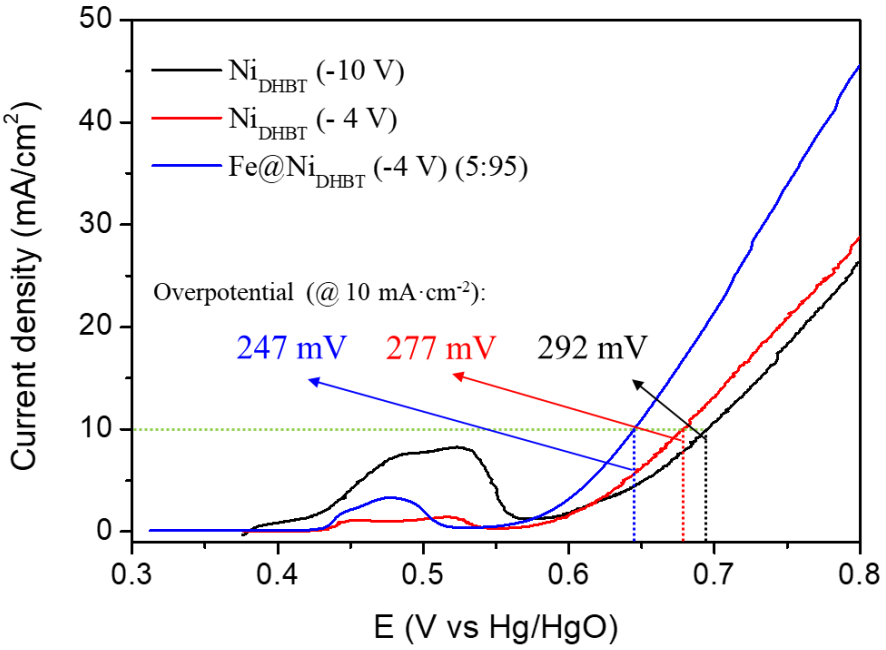

Figure 5.9 LSV results of the Ni$_{DHBT}$ (-10 V), Ni$_{DHBT}$ (-4 V), and Fe@Ni$_{DHBT}$ (-4 V) (5:95). Scan rate = 50 mV·s^{-1}; electrolyte = 1M KOH.

The improved OER activity of the Fe@Ni$_{DHBT}$ (-4 V) (5:95) catalyst was further confirmed by its smaller Tafel slope of 48.10 mV dec^{-1} compared to that of NIDHBT (-4 V) (63.30 mV dec^{-1}) and NIDHBT (-10 V) (131.76 mV dec^{-1}) in 1 M KOH (Figure 5.10).

After the calculation, the exchange current density of the Fe@Ni_{DHBT} (-4 V) (5:95) material described in this chapter was 1.89×10^{-7}A cm^{-2}. Compared to the calculated exchange current density (explained in Chapter 4) of the NMF-O_2/H_2 materials (2.51×10^{-5}A cm^{-2}), the value acquired from this Ni_{DHBT} materials is lower.

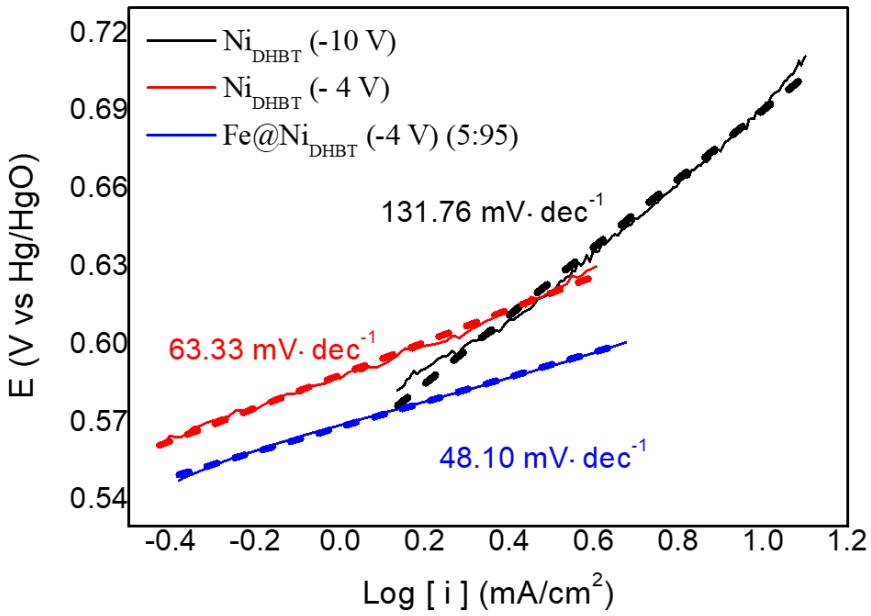

Figure 5.10 Tafel plots of Ni_{DHBT} (-10 V), Ni_{DHBT} (-4 V), and Fe@Ni_{DHBT} (-4 V) (5:95). Scan rate = 1 mV·s^{-1}; electrolyte = 1M KOH.

The Fe@Ni_{DHBT} (-4 V) (5:95) catalyst demonstrated a good operational durability in OER activity over a 1-hour continuous operation at a potential of 0.7 V (vs Hg/HgO) (Figure 5.11). Even when compared to Fe@NMF-O_2/H_2 (5:95), the results of the Fe@Ni_{DHBT} (-4 V) (5:95) were not good enough to maintain at a constant level; the drop of current density under 0.7 V was still in an acceptable range (27.1mA cm^2 – 22.2 mA cm^2). The decrease of the stability was due to the accumulation of the generated oxygen in the anodic section. Under the condition of no rotating electrode system being

applied, the accumulation of oxygen would have lowered the diffusion rate of the OH^- ion then decreased the reaction kinetics consequently. The decrease in the stability of the materials over 1 hour was 17%, which was due to the reaction kinetics reduction caused by the accumulation of the oxygen. The stability of the materials can be reported in an adequate range to be scaled up for usage.

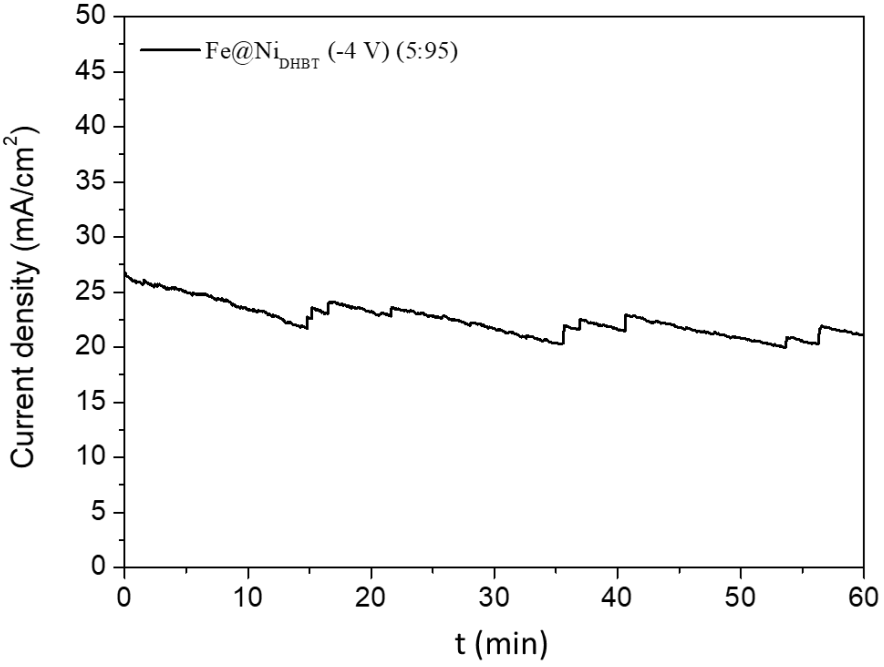

Figure 5.11 Stability test of Fe@Ni$_{DHBT}$ (-4 V) (5:95), under E = 0.7 V (vs Hg/HgO) for 1 hour in 1 M KOH.

5.4 Summary

By depositing a FeO_x colloid, we developed a series of Ni1.xFex/NC hybrid electrocatalysts which exhibit significantly improved OER activity in alkaline solution. The effect of Fe loading content on the electrocatalytic activities of Fe@NMF-O_2/H_2 and Fe@Ni$_{DHBT}$ electrocatalysts was also investigated. The results show that, for Fe@NMF-

O_2/H_2, Fe@NMF-O_2/H_2 (5:95) displayed the best performance in electrocatalyzing the OER. The overpotential to reach a current density of 10 mA cm^{-2} is about 262 mV. For the Fe@Ni_{DHBT} catalysts, the Fe@Ni_{DHBT} (-4 V) (5:95) shows the optimal OER activity with an overpotential of ~247 mV to achieve a current density of 10 mA·cm^{-2}.

Electrochemical results are collected and exhibited in table 5.4. From the electrochemical results listed in the table, both Fe@NMF-O_2/H_2 (5:95) and Fe@Ni_{DHBT} (-4 V) (5:95) shows promising catalytic capabilities and potentials to be further discussed and applied in fuel cell tests.

Table 5.4 Collection of electrochemical results

Catalysts	**Tafel slope (**mV.dec^{-1}**)**	**Overpotential (**mV**)**	**Exchange current density (**A cm^{-2}**)**
Fe@NMF-O_2/H_2 (5:95)	41.90	262	1.64×10^{-7}
Fe@Ni_{DHBT} (-4 V) (5:95)	48.10	247	1.89×10^{-7}

5.5 Reference

[1]. Roger, I., & Symes, M. D. (2015). Efficient Electrocatalytic Water Oxidation at Neutral and High pH by Adventitious Nickel at Nanomolar Concentrations. Journal of the American Chemical Society, 137(43), 13980–13988.

[2]. Lu, X., & Zhao, C. (2015). Electrodeposition of hierarchically structured three-dimensional nickel-iron electrodes for efficient oxygen evolution at high current densities. Nature Communications, 6.

[3]. Zhao, Z., Wu, H., He, H., Xu, X., & Jin, Y. (2015). Self-standing non-noble metal (Ni-Fe) oxide nanotube array anode catalysts with synergistic reactivity for high-performance water oxidation. Journal of Materials Chemistry A, 3(13), 7179–7186.

[4]. Bau, J. A., Luber, E. J., & Buriak, J. M. (2015). Oxygen Evolution Catalyzed by Nickel-Iron Oxide Nanocrystals with a Nonequilibrium Phase. ACS Applied Materials and Interfaces, 7(35), 19755–19763.

[5]. Xing, J., Li, H., Ming-Cheng Cheng, M., Geyer, S. M., & Ng, K. Y. S. (2016). Electro-synthesis of 3D porous hierarchical Ni-Fe phosphate film/Ni foam as a high-efficiency bifunctional electrocatalyst for overall water splitting. Journal of Materials Chemistry A, 4(36), 13866–13873.

[6]. Wang, J., Ji, L., & Chen, Z. (2016). In Situ Rapid Formation of a Nickel-Iron-Based Electrocatalyst for Water Oxidation. ACS Catalysis, 6(10), 6987–6992.

[7]. Panaritis, C., Zgheib, J., Ebrahim, S. A. H., Couillard, M., & Baranova, E. A. (2020). Electrochemical in-situ activation of Fe-oxide nanowires for the reverse water gas shift reaction. Applied Catalysis B: Environmental, 269(February), 118826.

Chapter 6 – Conclusion and future works

6.1 Summary of the Thesis Conclusions

The focus of this research was to develop 3D porous Ni-based OER catalysts for the water splitting process. A series of 3D structured porous Ni foam electrocatalysts was developed using a facile one-pot reflux method. The materials were characterized by SEM imaging and were found to possess abundant nano-sized pores and cracks on the surface of the Ni wires. The effect of different surface treatments (e.g. under H_2 reduction or O_2 oxidation) on the catalytic activity of NMF materials was systematically studied. The results show that the Ni foam that was obtained by successive O_2 oxidation/H_2 reduction exhibits the best OER activity. It exhibits a low OER overpotential (~364 mV) when a current density of 10 mA cm^{-2} is generated in alkaline media.

Since $Ni(OH)_2$ is usually considered an active species toward the OER, porous $Ni/Ni(OH)_2$ catalysts were also fabricated using the dynamic hydrogen bubble templating electrodeposition and etching method. The effect of electrodeposition potentials on the morphology and electrochemical performance of $Ni/Ni(OH)_2$ was investigated. The results show that the Ni_{DHBT} (-4 V) exhibits better OER activity than Ni_{DHBT} (-10 V) does, with a lower overpotential at 277 mV compared to 292 mV at 10 mA cm^{-2}. The results suggest that a porous $Ni(OH)_2$ design is an effective strategy for developing efficient OER catalysts.

Finally, on the basis of the high catalytic activity of NMF-O_2/H_2 and Ni_{DHBT}, Fe component was deposited on their surface to evaluate its effect on the OER activity. The

resulting products are porous structured FeO_x-Nickel meso-foam (Fe-NMF) and FeO_x-Ni/$Ni(OH)_2$-layered structure materials (Fe-Ni_{DHBT}). The optimized Fe@NMF-O_2/H_2 (5:95) catalyst exhibits an overpotential of 262 mV at a current density of 10 $mAcm^{-2}$, much lower than that of the NMF-O_2/H_2 (364 mV). Similarly, the FeO_x-Ni/Ni $(OH)_2$ catalyst also shows enhanced OER activity with a lower overpotential of 247mV than that of Fe-Ni_{DHBT} (277 mV). In addition to the improved OER activity, the Fe deposited catalysts also show good stability, revealing that Fe deposition is beneficial for improving the OER performance of Ni foam-based catalysts.

Table 6.1 Comparisons of all tested materials towards OER catalysis

	Current density (@0.8 V) ($mA\ cm^{-2}$)	**Overpotential (@10$mA\ cm^{-2}$) (mV)**	**Tafel slope ($mV\ dec^{-1}$)**
NMF-O_2/H_2	**16.72**	**364**	**62.91**
Ni_{DHBT}	**27.47**	**277**	**63.33**
Fe@ NMF-O_2/H_2	**39.15**	**262**	**45.40**
Fe@Ni_{DHBT}	**44.98**	**247**	**48.10**

6.2 Future works

This research represents a rational design and development of efficient Ni foam-based OER catalysts in water splitting. The effect of surface treatment, porous structure design, and Fe deposition on the OER activities was systematically studied, which provides

guidance for the development of Ni-based OER catalysts. However, there are still many challenges ahead for the development of high performance OER electrocatalysts. The following are recommendations for future research.

1) The synergistic or deposition effects of other M-Ni (M = Co, etc.) on OER activity

The present study has shown that the introduction of Fe would significantly improve the OER activity of Ni foam-based catalysts. Since Co is also a well-known component that usually exhibits excellent activity towards OER, the introduction of Co or other transition metals into the as-developed NMF-O_2/H_2 and Ni_{DHBT} catalysts to further evaluate its OER activity and synergistic effects would be useful for future research. In addition to the M-Ni binary catalysts, the development and study of Ni foam-based ternary OER catalysts might provide a more comprehensive picture of this field.

2) Overall performance in water splitting

In this study, only the OER activity was evaluated in a half-cell set-up. The study of the actual performance of these fabricated catalysts in fuel cells would be useful. Of course, this would require an efficient HER catalyst, and therefore, the development of Ni foam-based HER or HER-OER bi-functional catalysts would also be a promising topic.